Experimental Techniques for Static and Dynamic Analysis of Thick Bonding Wires

by

Resul Saritas

A thesis
presented to the University of Waterloo
in fulfillment of the
thesis requirement for the degree of
Master of Applied Science
in
Mechanical Engineering

Waterloo, Ontario, Canada, 2015

I hereby declare that I am the sole author of this thesis. This is a true copy of the thesis, including any required final revisions, as accepted by my examiners.

I understand that my thesis may be made electronically available to the public.

ABSTRACT

Thick bonding wires are used in modern power modules as connectors between integrated circuits, carrying current from one circuit to another. They experience high values of current, which generates heat through Joule heating and can lead to various failure mechanisms. Typically used wire materials in industry are aluminum (Al), copper (Cu), and intermetallic compounds of Cu-Al. They are broadly used because of their strength, high thermal conductivity, and low resistivity.

This study reports on the influence of thermal loading on the mechanical behavior of bonding wires. Experimental techniques are developed and introduced in this thesis to analyze quasi-static and dynamic response of bonding wires $300\mu m$ in diameter. First, an experimental technique is developed to measure the quasi-static displacement of bonding wires carrying DC currents. It is then deployed to measure the displacement, as well as peak temperature, of three types of bonding wires, Al, Cu and Aluminum coated Copper (CuCorAl) to study the response under DC current.

Secondly, an experimental technique is established and deployed for modal analysis of bonding wires under thermal loading. Experimental results demonstrate a drop in the natural frequency of bonding wires with increased thermal loads. Moreover, a harmonic analysis technique using thermal excitation is developed and applied to analyze the mode shapes and frequency response of bonding wires.

Furthermore, an analytical model and a finite element model are used to analyze static and dynamic responses of bonding wires. Numerical and experimental results are compared in this thesis.

Acknowledgements

Dedication

To my dear parents and brother...

Contents

List of Tables

List of Figures

Chapter 1

Introduction

1.1 Motivation

The integrity of power modules, such as Insulated Gate Bipolar Transistors (IGBT), is a critical issue because of high voltage or current involved in electrical energy transfer. Bonding wires have been widely used as connectors to transfer power between integrated circuits in IGBT modules. The high current carried by these wires causes joule heating and results in thermal stress as temperature rises. To improve reliability bonding wires made of high conductivity materials, such as Al, Cu, gold (Au), intermetalic compounds and alloys of Cu-Al, have been used in industry.

Thermal stress is a main reason of failure in bonding wires. Thermal cycles or time varying current causes cyclic stress in wires driving fatigue failure mechanism. External excitation for the bonding wire in one of its resonant frequencies causes maximum deflection in the wire which accelerates wire fatigue. In this thesis, we develop experimental methods analysis to determine the maximum displacement and temperature in the wires. We also develop techniques for modal and harmonic analysis to determine the natural frequencies, mode shapes and frequency response of bonding wires. Moreover, we investigate the effect of thermal loading on mechanical behavior of bonding wire.

In this chapter, a general overlook of bonding wires is presented. We also

reviewed state of the art on bonding wire reliability.

1.2   Classification of Bonding Wires

Demand on bonding wires have been increasing in industry, despite the availability of other alternatives, for example, flip-chip assembly [1]. It is reported that more than 4 trillion bonding wires are made annually [2]. Bonding wires have been called according to bonding method: ultrasonic, thermocompression and thermosonic [1]. **Ultrasonic wire bonding (US)**: are bonded without applying an external thermal load, thus this method is considered a proper way to connect integrated circuits [3]. Wedge-wedge bonding for wires with diameter in range 75-500 μm is mostly used in high power applications such as IGBT modules [1]. Figure 1.1 shows ultrasonic wedge wire bonding. important advantages of ultrasonic bonding are that Al wire is bonded at room temperature and wires can be produced down to 50 μm pitch [4]. Figure 1.2 shows a closer view of bonded surface.
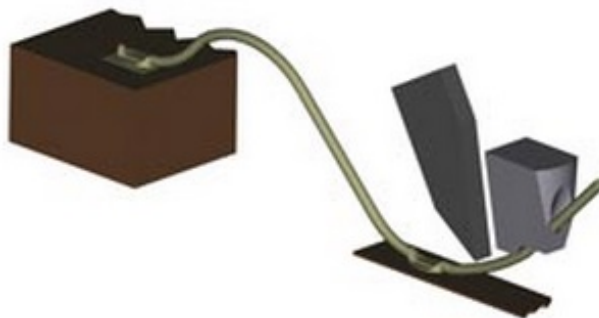
Figure 1.1: Ultrasonic wedge bonding [4]

Thermocompression wire bonding (TC): is introduced by Bell Laboratories in 1957. It requires high temperature, approximately $300°C$, which is a high interface temperature for microelectronics, thus this method is rarely used in microelectronics [5]. The most attractive advantage of this method is that it is very reliable for Au-Au bonding. Its disadvantages are, high interface temperature, higher risk of contamination than TS or US methods and lower yield than those two methods [5].

Figure 1.2: Close view of wedge bonding [5]

Thermosonic wire bonding (TS): was firstly used in 1970. It is a composite of ultrasonic energy and thermocompression. An advantage of using TS bonding is that it requires lower energy compared with US [5]. Figure 1.3 illustrates a process of ball and stitch bonding [1], and Figure 1.4 shows a close view of ball bonded surface [6]. Thermosonic wire ball bonding is mostly applied to Cu) and Au wires [7].
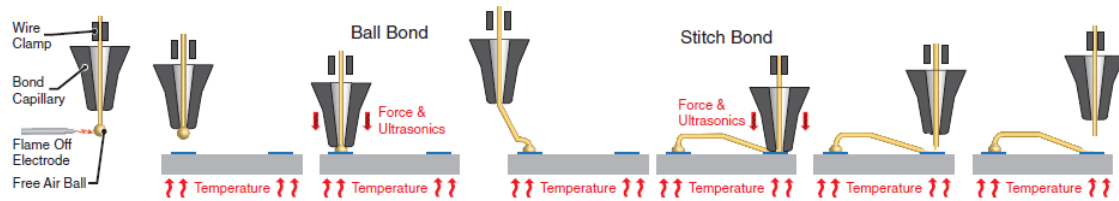
Figure 1.3: Process of thermosonic bonding [1]

Wire bonds are also classified into thin and thick wire bonds. Thin wires vary in diameter between 20- 100μm, while thick wires have diameters between 100-500μm. The choice of bonding wire diameter depends on application based on amount of power transfered. Further, scaling down of electronics and introduction of NEMS is increasing interest in down scaling of thin bonding wires towards the nano scale [8]. Usually bonding wires are produced curved and asymmetric for design purposes.
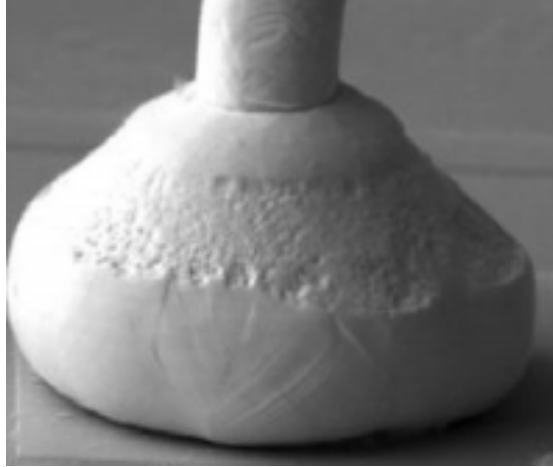
Figure 1.4: Close view of ball bonding [6]

Figure 1.5 shows a schematic of bonding wire, where L is wire loop length and h is loop height.
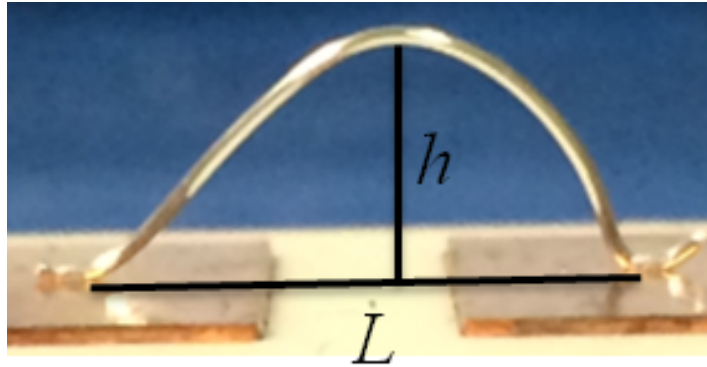
Figure 1.5: A picture of bonding wire

1.3 Materials of Bonding Wires/Pads

Various materials have been used for bonding wire, each having its own advantages and disadvantages [1]. As mentioned before, Al, Cu, Al-Cu and Au have been used because of their high thermal conductivity and low resistivity [8]. Copper seems to be the most attractive material due to higher thermal conductivity compared with other materials mentioned above and a reasonable cost [9].

Various combinations wire-pad intermetallic bonds have been implemented in-

cluding: Au-Al, Cu-Al, Ag-Al, Al-Ni, Al-Al, Au-Au, Au-Ag and Cu-Au [5, 11]. They have various advantages, for example it is easier to form Au-Al bonds compared to Cu-Al bonds because atomic size difference between Cu and Al is larger than that between Au and Al [10]. Likewise, Figure 1.6 demonstrates that Cu-Au bonds have better thermal aging properties than Cu-Al bonds [11].
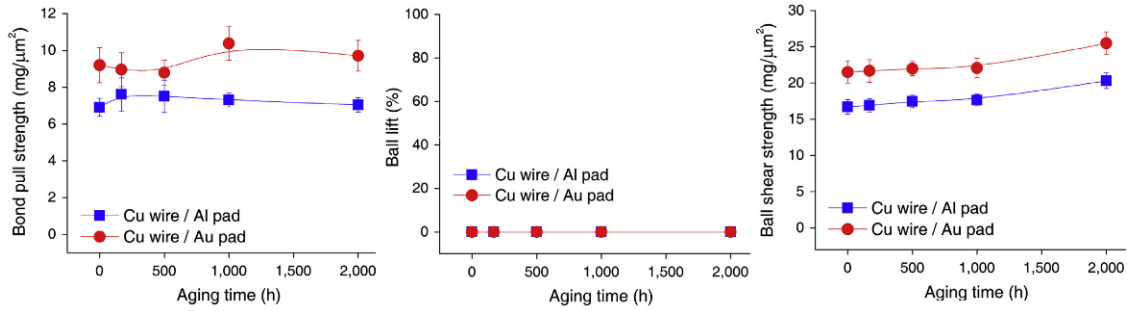
Figure 1.6: Thermal aging properties of Cu wire bonding with Al and Au pads [11]

Moreover, other wire-pad combinations have been introduced, for example: Pd-Al, Pt-Pt, Ni-SiC and Ag-SiC [1]. Insulated wire, called X-Wire^{TM} [12], is used in complex package design [12]. It allows wires to cross and touch each other.

1.4   Failure Mechanisms

Wire bonding is an essential step in electronics packaging, especially for IGBT modules, Figure 1.7, transferring power between integrated circuits [8]. Wires are exposed to high power leading to different reported failure mechanisms [6, 13].

- Lift off failure

- Heel crack failure

- Wire failure near the die pad

- DBC substrate cracking failure

- Wire failure near the frame
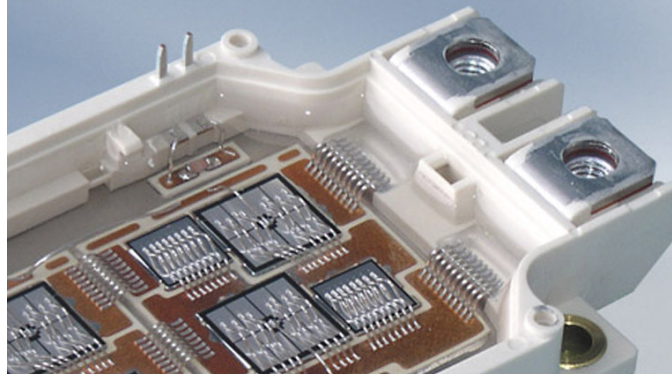
Figure 1.7: An IGBT module[14]

The most frequent failures are lift-off and heel crack[8]. They are described as follows:

- **Lift-off**: Materials used in bonding wires and in chips are not usually same, and it leads to mismatch in the Thermal Expansion Coefficients (TEC) of bonding wires and chips. For example, TEC for aluminum bonding wire is $\sim 24 \times 10^{-6}/\text{K}$, while TEC for a silicon chip is $\sim 3 \times 10^{-6}/\text{K}$. When aluminum wire - silicon chip system is heated up, the boundary between wire and chip experiences shear stress, which causes crack between two layers. Figure 1.8 shows a crack growing between the two layers and a close view of the crack. Eventually the crack expands and leads to lift off failure [15].
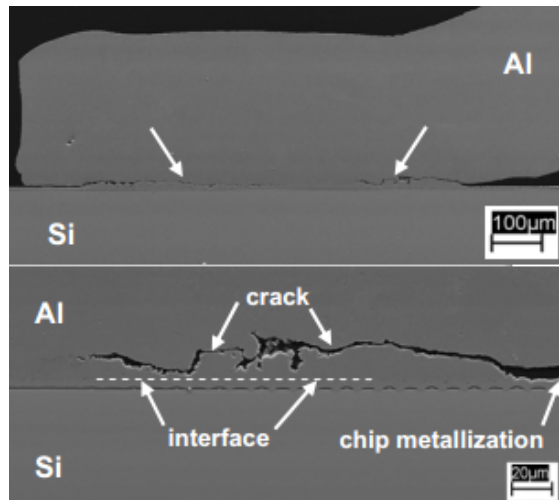
Figure 1.8: Crack at interface [15]

Yamada et al. [16] presented such a crack growing on both sides of the heel area towards the center in Si-Al bonds and showed decrease in bonding length as function of the number of thermal cycles, Figure 1.9. Figure 1.10 shows a general view of wire lift-off failure in a IGBT module [17].
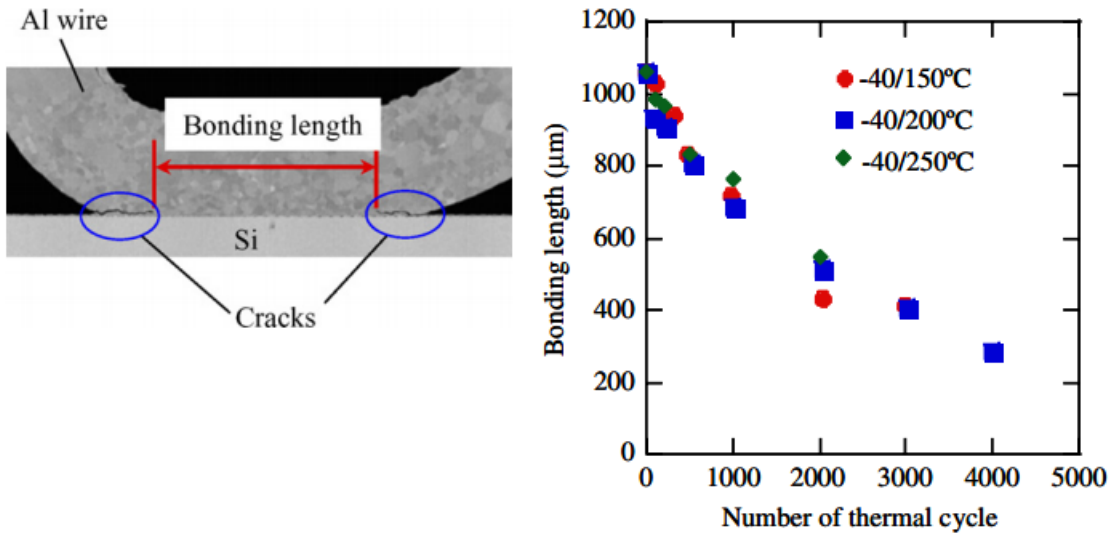
Figure 1.9: Decrease in bonding length as function of thermal cycles [16]
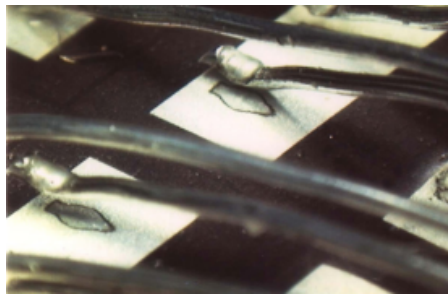
Figure 1.10: Wire lift-off failure [17]

Loh et al. [18] reported heel crack growth of Al wire bonds with at different bonding temperatures (25-100-200 °C). Figure 1.11 points out change in the bonding interface of wires at different bonded temperatures after 1500 thermal cycles.

Loh et al. [18] introduced in Figure 1.11, bonding process in high temperature results in recovery or recrystallization of grains. It clearly seems that grain size becomes increasing under higher temperature bonding process, which slows
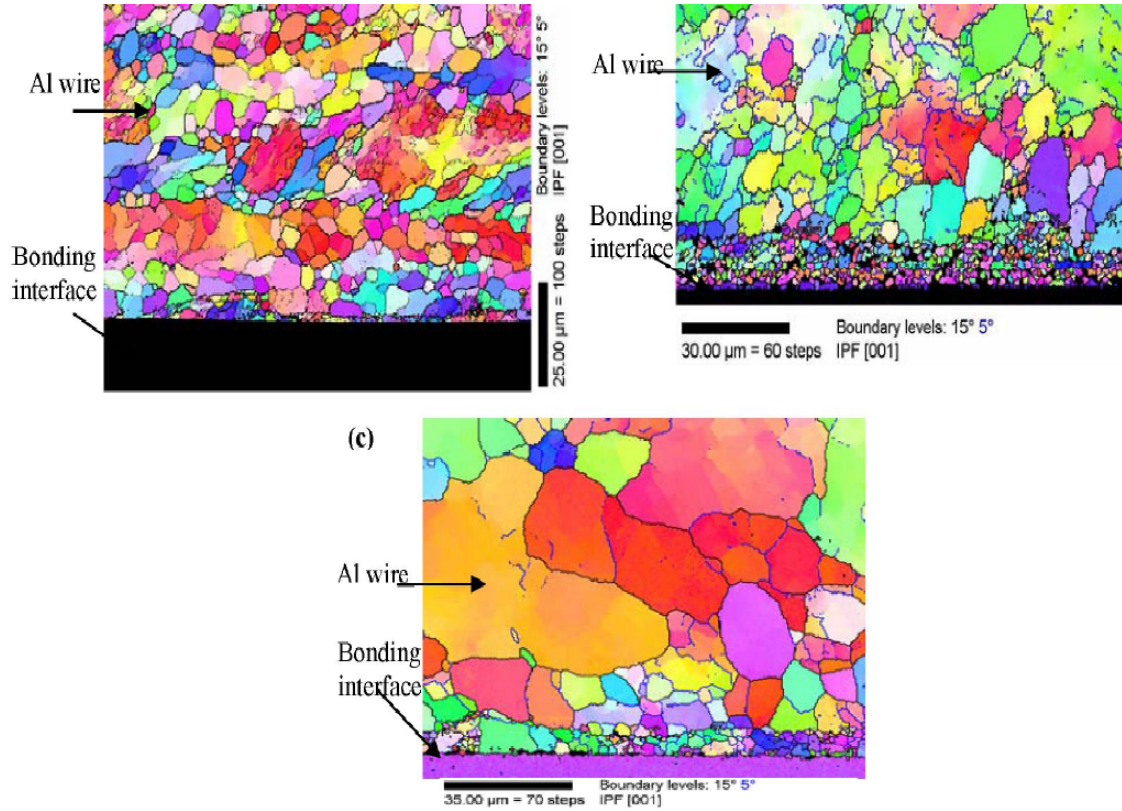
Figure 1.11: Change in bonding interface at 25-100-200 °C bonding temperatures [18]

down crack propagation along bonding interface due to mismatching thermal expansion coefficient [18]. This case is always desired in IGBT modules in terms of reliability.

- **Heel Cracking**; is one of the main failure mechanisms. For ultrasonically wedge bonded wires, using a sharp bonding tool may cause initial heel cracks when bonding tool is moved up from the first bonded side [5]. Further, rapid tool motion may cause of cracks. Moreover, to achieve desirable high loops, heel of bonding wires is exposed to more mechanical stress by tool movement during fabrication. Thus, heel of wire already is weakened in the fabrication process [5]. Moreover, another crack type is caused by auto bonding process and vibrations. It is observed that as the bottom of the heel becomes brittle cracks occur there also [5]. Figure 1.12 shows a crack developing at the bottom of the heel.
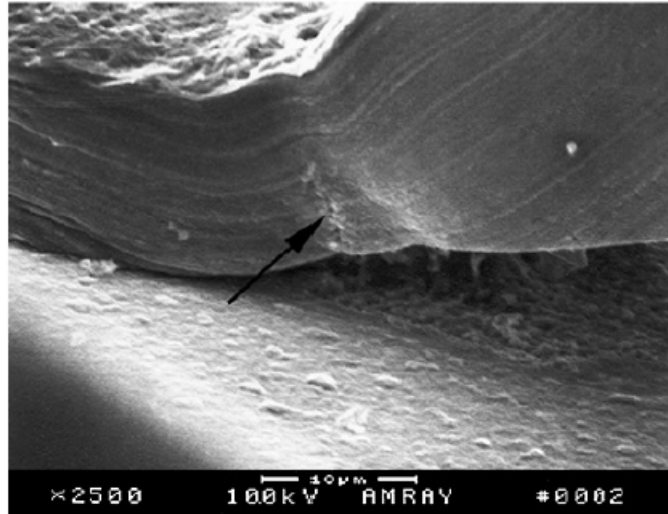
Figure 1.12: Crack under bottom of heel [5]

Furthermore, time varying power cycles causes wires to expand upward and backward, which causes thermal stress cycles resulting in cracks in the heel of the wire. Figure 1.13 shows such a crack failure after 10^7 power cycles [19].
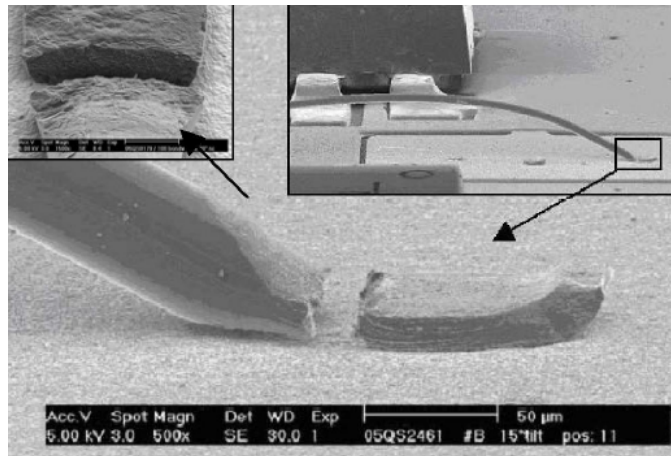
Figure 1.13: Heel crack caused by 10^7 cycles of thermal stress [19]

1.5 Life Time Estimation

Thermal, power and mechanical cycling methods have been reported to estimate life time of bonding wires. Matsunaga et al[20] introduced that thermal cycling period varying from 2 to 3 seconds, and temperature swing range ΔT varying from

9

50 to $120K$ are suitable conditions that can be applied to assess life time of bonding wires using fast thermal cycling test. Figure 1.14 shows effect of applied time period for thermal cycling stress for bonding wires.
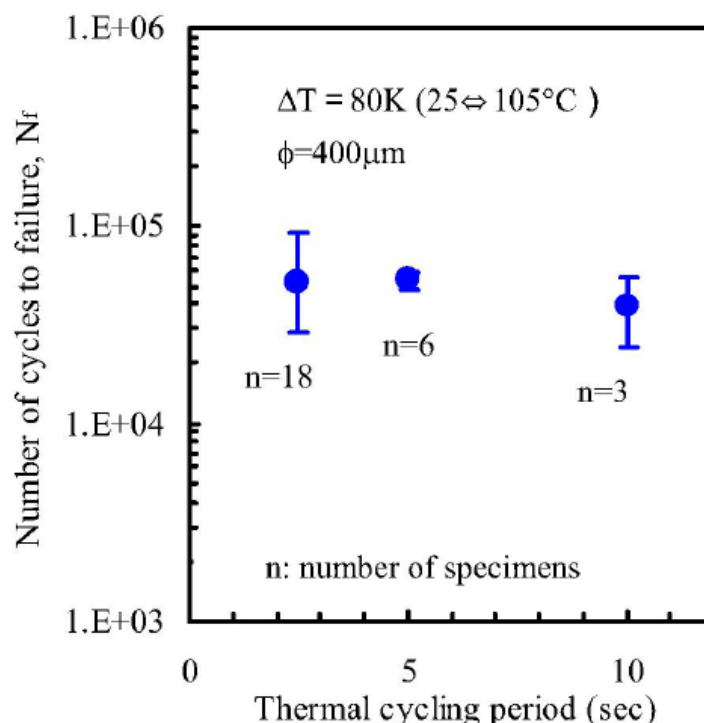
Figure 1.14: Effect of applied period for thermal cycling stress [20]

According to Figure 1.14, when life time observed, the time period of 2.5s is reasonably same with case 5s however, in case of 10s, there is 25% off to compare with 2.5s, thus applying such a long time thermal cycling period (10s) may not give accurate life time estimation for bonding wires [20]. Moreover; Schmidt et al[21] proposed that power cycling test can be used to separate different failure mechanisms such as pure lift-off and heel cracking. Figure 1.15 illustrates aspect ratio effect for different failure mechanism.

According to Figure 1.15 Increasing aspect ratio of bonding wires reveals that bonding wires can resist more power cycles, and it changes failure mechanism from heel cracking to lift-off [21]. Moreover, for low aspect ratio, heel cracking and lift-off failure occurs almost at same number of power cycles for Ag-sintered and soldered modules, however with high aspect ratio, Ag-sintered modules seems more
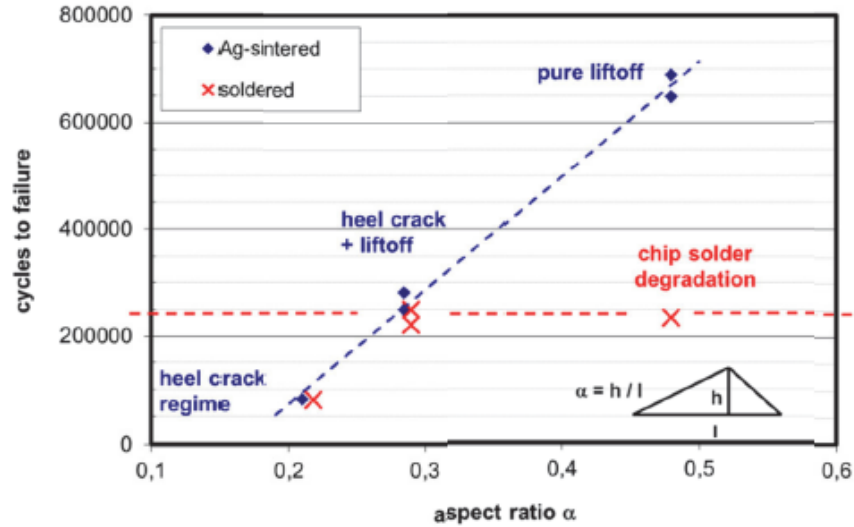
Figure 1.15: Effect of aspect ratio for different failure mechanisms [21]

promising to compare with solder modules while soldered modules fail due to chip solder degradation [21].
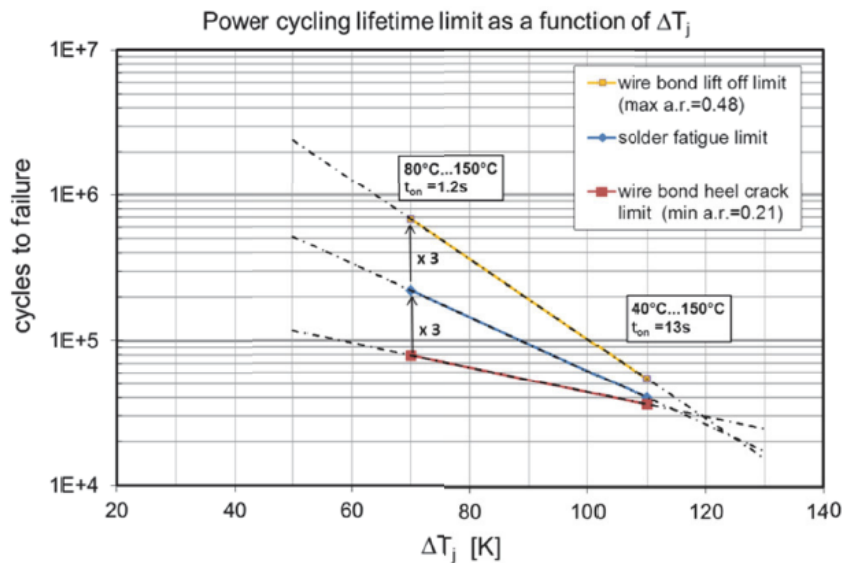
Figure 1.16: Effect of ΔT_j for different failure mechanisms [21]

Also, Figure 1.16 demonstrates lifetime limits of different failure mechanisms as function of junction temperature swings ΔT_j [21]. Based on results shown in Figure 1.16, with high aspect ratio, changes in ΔT_j cause a significant drop in lifetime estimation of lift-off failure mechanism, and heel cracking failure with low aspect

ratio not depends on ΔT_j same as lift-off failure [21]. In addition, Merkle et al. [22] presented an approach to estimate life time of bonding wires using mechanical cycling method.

According to Merkle's experimental results, bonding wires with higher heights can resist to higher number of cycles to failure. Also, some studies reported analytical models to predict life time for bonding wires such as, Ciappa et al. [23] presented an analytical approach to estimate a mean average life time of bonding wires assuming degradation occurring linearly under thermal cyclic loads. In addition, Hu et al. [24] reported an analytical approach for thermal fatigue life time and reliability estimation of bonding wires. Based on Hu's results, uncertainties which are because of temperature waves such as stress amplitude and life time estimation of bonding wires are obtained.

Chapter 2

Model

2.1 Model for In-Plane Vibration

Many investigators have analyzed curved beams and circular rings. Wang et al. [28] proposed an analytical method to determine the natural frequencies and mode shapes of circular rings with a known central angle. Likewise, Irie et al. [29] reported on the natural frequencies of out-of-plane vibration modes of circular rings using Timoshenko beam theory and taking into account shear deformation and rotary inertia.

Laura et al. [25] introduced an approach to obtain the first two natural frequencies of hinged and clamped arches with linearly varying thickness using Rayleigh-Ritz method. Yang et al. [26] used extended Hamilton principle to obtain the governing equation of motion for curved beams, then applied the finite element method to solve problem. They showed that their approach matches published results for circular, sinusoidal, parabolic and elliptical beams. Tarnopolskaya et al. [27] analyzed free in-plane vibrations of curved beams with variable curvature and cross-sectional area using a perturbation technique. They presented results for bending mode transition as the beam curvature increased.

Lacarbonara [30] analyzed the nonlinear vibrations of geometrically imperfect beams using Euler-Bernoulli beam theory and assuming shear deformation, longitudinal inertia and rotary inertia negligible. He applied Hamilton principle to

derive the equation of motion for the beams. Further, this model was extended by Emam [32] and Khater et al. [31] to include time-varying thermal and residual stresses.

In this work, we adopt a curved beam model with a uniform circular cross-section to represent bonding wire. We assume a symmetric bonding wire as shown schematically in Figure 2.1.
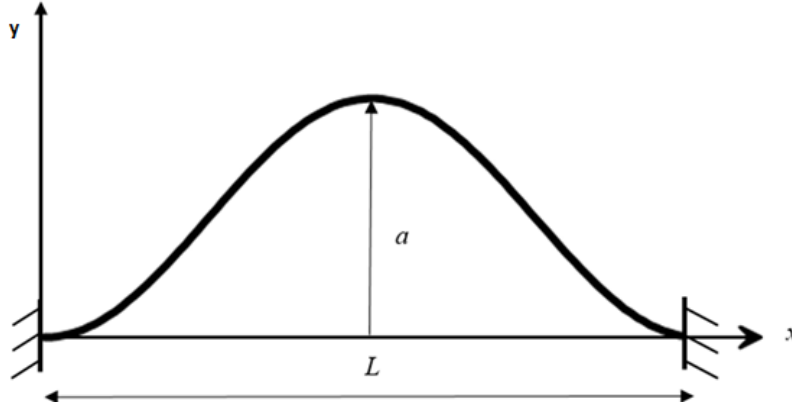
Figure 2.1: A schematic of the bonding wire

Where L is wire length and a is the midspan wire rise. Axial strain due to axial load $P(t)$ and mid-plane stretching, can be written as [30]

$$\epsilon_\circ = u' + w'_\circ w' + \tfrac{1}{2}w'^2 \qquad (2.1)$$

where $u(x,t)$ and $w(x,t)$ are components of the displacement field along the x- and y-directions, respectively, $w_\circ(x)$ is the initial shape of the curved wire, and the prime stands for the derivative with respect to x. The axial strain due to bending caused by the external transverse force $F(x,t)$ can be written as

$$\epsilon_f = EIw'' \qquad (2.2)$$

where EI is the bending stiffness (flexural rigidity) of the beam section. The strain caused by thermal loads is

$$\epsilon_t = \alpha\Delta T \qquad (2.3)$$

14

where α, is the thermal expansion coefficient and $\Delta T(x,t)$ is the temperature difference between the beam and environment.

The total axial strain can then be written as [30];

$$\epsilon = \epsilon_\circ - \epsilon_f - \epsilon_t \tag{2.4}$$

$$\epsilon = u' + w'_\circ w' + 1/2 w'^2 - EIw'' - \alpha \Delta T \tag{2.5}$$

The total potential energy of the wire can be written as

$$V = \frac{1}{2}\int_0^l \int_A E\epsilon^2 \, dA \mathrm{d}x - \int_0^l Fw \, \mathrm{d}x + Pu(l,t) \tag{2.6}$$

where l is the length of wire. The kinetic energy of the wire is;

$$T = \frac{1}{2}\int_0^l m(\dot{u}^2 + \dot{w}^2) \, \mathrm{d}x \tag{2.7}$$

where m is the wire mass per unit length and the overdot stands for the derivative with respect to time.

The extended Hamilton principle can be written as

$$\int_{t_0}^{t_f} (\delta T - \delta V) \, \mathrm{d}x = 0 \tag{2.8}$$

Substituting with Eqs. (2.6) and (2.7) into Eq. (2.8), taking the variation of the kinetic and potential energies, and setting the integrand equal to zero, we obtain a partial differential equation describing the in-plane transverse vibrations due to an external axial force $P(t)$, an external transverse force $F(x,t)$, and a thermal load $\Delta T(x)$ [30, 31, 33]

$$\begin{aligned}
\rho A \frac{\partial^2 w}{\partial t^2} + c\frac{\partial w}{\partial t} + EI\frac{\partial^4 w}{\partial x^4} + P\left[\frac{\partial^2 w}{\partial x^2} + \frac{\partial^2 w_\circ}{\partial x^2}\right] + \frac{EA}{L}u_{th}\left[\frac{\partial^2 w}{\partial x^2} + \frac{\partial^2 w_\circ}{\partial x^2}\right] \\
- \frac{EA}{2L}\left[\frac{\partial^2 w}{\partial x^2} + \frac{\partial^2 w_\circ}{\partial x^2}\right]\int_0^l \left[\left(\frac{\partial w}{\partial x}\right)^2 + 2\frac{\partial w}{\partial x}\frac{\partial w_\circ}{\partial x}\right] \mathrm{d}x = 0
\end{aligned} \tag{2.9}$$

where ρ is density, A and I are the cross sectional area and second moment of area,

E is Young's Modulus, and c is the viscous damping coefficient. The axial strain due to thermal loading is

$$u_{th} = \int_0^l \alpha \Delta T \, \mathrm{d}x \tag{2.10}$$

Further, the wire is modeled as a clamped-clamped beam with the boundary conditions:

$$w(0, t) = 0$$
$$w(l, t) = 0$$
$$\frac{\partial w}{\partial x}(0, t) = 0 \tag{2.11}$$
$$\frac{\partial w}{\partial x}(l, t) = 0$$

We non-dimensionalize the equation of motion, thereby simplifying it and lumping the system parameters into a few non-dimensional groups, by introducing the non-dimensional variables

$$x = \frac{x}{l}, \quad w_\circ = \frac{w_\circ}{r}, \quad w = \frac{w}{r}, \quad t = \frac{t}{T} \tag{2.12}$$

where r is the section radius of gyration and T is a time scale. Since the wire cross section is circular

$$r = \frac{1}{4}d$$

where d is the wire diameter. Introducing these variables into Eqs. (2.9) and (2.11) yields [31]

$$\frac{\partial^2 w}{\partial t^2} + c\frac{\partial w}{\partial t} + \frac{\partial^4 w}{\partial x^4} + \alpha_1 P_\circ \left[\frac{\partial^2 w}{\partial x^2} + \frac{\partial^2 w_\circ}{\partial x^2} \right] + \alpha_2 u_{th} \left[\frac{\partial^2 w}{\partial x^2} + \frac{\partial^2 w_\circ}{\partial x^2} \right]$$
$$- 2\left[\frac{\partial^2 w}{\partial x^2} + \frac{\partial^2 w_\circ}{\partial x^2} \right] \int_0^l \left[\left(\frac{\partial w}{\partial x} \right)^2 + 2\frac{\partial w}{\partial x}\frac{\partial w_\circ}{\partial x} \right] \mathrm{d}x = 0 \tag{2.13}$$

and the boundary conditions,

$$w(0, t) = 0 \,, \quad w(1, t) = 0 \,, \quad \frac{\partial w}{\partial x}(0, t) = 0 \,, \quad \frac{\partial w}{\partial x}(1, t) = 0 \tag{2.14}$$

where

$$c = \frac{cl^2}{\sqrt{\rho A E I}}, \quad T = \sqrt{\frac{\rho A E I}{r}}, \quad \alpha_1 = \frac{l^2}{EI}, \quad \alpha_2 = \frac{4l^2}{r^2} \tag{2.15}$$

The initial wire shape is approximated as a symmetric dome given by

$$w_\circ = \frac{1}{2}a(1 - cos2\pi x) \tag{2.16}$$

where a is the rise at the wire midspan due to initial curvature. To solve Eq. (2.13), we use a reduced-order model (ROM) where the in-plane response is assumed as [34];

$$w(x,t) = \sum_{i=1}^{n} \phi_i(x)u_i(t) \tag{2.17}$$

where the response has been decomposed into two components: a space-dependent term $\phi_i(x)$ which represents the wire mode shape and a time dependent term $u_i(t)$ to account for the time variation in wire displacement. Reduced-order models reduce the system dimension and, accordingly, computational complexity and cost. On the other hand, since we are taking the effects of initial curvature and mid-plane stretching into account, the model should be able to accurately capture moderately large vibration of bonding wire [34];.

A first step in solving Eq. (2.13) is to find the wire mode shapes. We solve the linear, undamped, free vibrations problem obtained by dropping the damping, forcing, and nonlinear terms from the equation. The result is

$$\frac{\partial^2 w}{\partial t^2} + \frac{\partial^4 w}{\partial x^4} + N\left[\frac{\partial^2 w}{\partial x^2} + \frac{\partial^2 w_\circ}{\partial x^2}\right] - 4\frac{\partial^2 w_\circ}{\partial x^2}\int_0^l \left(\frac{\partial w}{\partial x}\frac{\partial w_\circ}{\partial x}\right) \mathrm{d}x = 0 \tag{2.18}$$

where $N = \alpha_1 P_\circ + \alpha_2 u_{th}$ represents the axial stress within the wire before transverse loading. Solution of Eq. (2.18) is obtained by assuming the solution form

$$w(x,t) = \phi(x)e^{i\omega t}$$

17

and substituting into the equation to get

$$\phi^{iv} + N\phi'' u_i - 4w_0'' \int_0^1 \phi' w_o' dx = \omega^2 \phi \tag{2.19}$$

which can be simplified using Eq. (2.16) to

$$\phi^{iv} + N\phi'' - \omega^2 \phi = 8a^2 \pi^3 cos(2\pi x) \int_0^1 \phi' sin(2\pi x) dx \tag{2.20}$$

subject to the boundary conditions

$$\phi(0) = 0 , \quad \phi(1) = 0 , \quad \phi'(0) = 0 , \quad \phi'(1) = 0 \tag{2.21}$$

The solution of Eq. (2.20) is composed of a homogeneous part, $\phi_h(x)$, and a particular part, $\phi_p(x)$. The homogeneous solution takes the form [30, 32, 35]

$$\phi_h(x) = c_1 sin(\beta_1 x) + c_2 sin(\beta_1 x) + c_3 sinh(\beta_2 x) + c_4 sin(\beta_2 x) \tag{2.22}$$

where

$$\beta_1 = \sqrt{-\frac{N}{2} + \sqrt{\frac{1}{4}N^2 + \omega^2}} , \quad \beta_2 = \sqrt{\frac{N}{2} + \sqrt{\frac{1}{4}N^2 + \omega^2}} \tag{2.23}$$

In view of Eq. (2.20), the particular solution is assumed in the form

$$\phi_p(x) = c_5 cos(2\pi x)$$

Thus we can write

$$\phi(x) = c_1 sin(\beta_1 x) + c_2 sin(\beta_1 x) + c_3 sinh(\beta_2 x) + c_4 sin(\beta_2 x) + c_5 cos(2\pi x) \tag{2.24}$$

Applying the boundary conditions, Eq. (2.21), to $\phi_h(x)$ gives four equations in the constants $c_1 - c_4$ and ω, which can be solved for the natural frequencies and the corresponding mode shapes. Substituting the particular solution in Eq. (2.20), we obtain c_5.
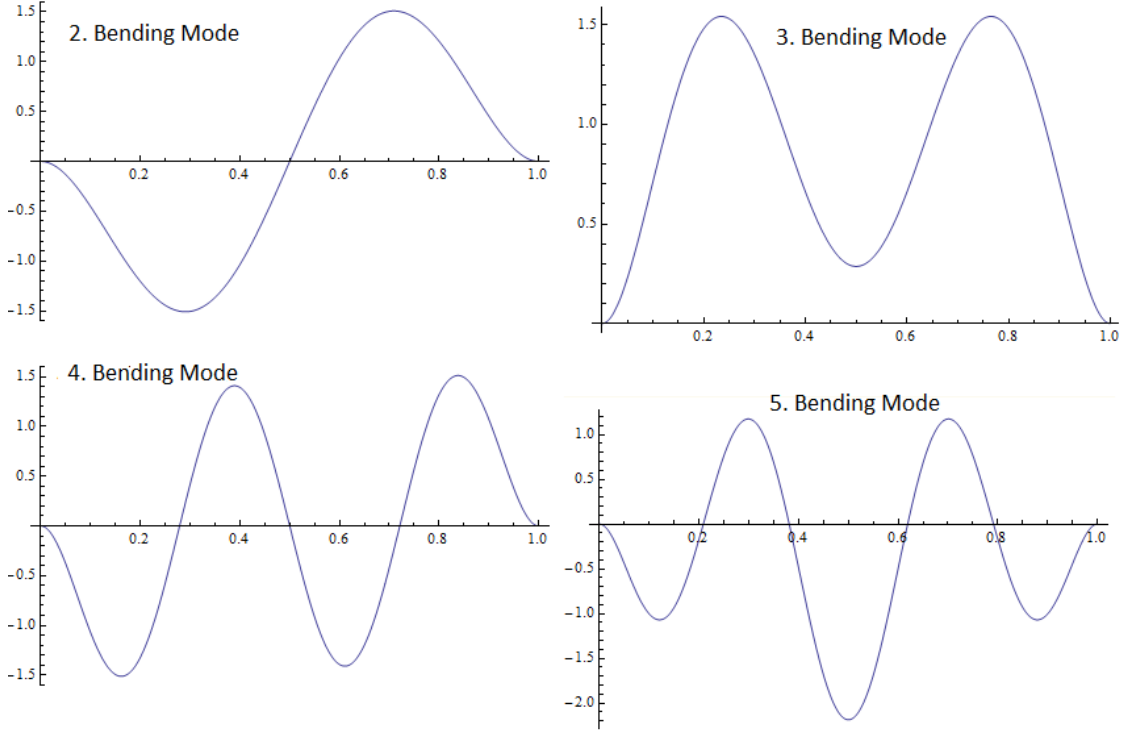
Figure 2.2: Mode shapes of the wire bonding

Figure 2.2 shows the in-plane bending mode shapes of the wire obtained from this analytical model. The Figure 2.2 shows the second, third, fourth and fifth bending modes appearing at $\Omega_2 = 26.7$ kHz, $\Omega_3 = 36.5$ kHz, $\Omega_4 = 87.1$ kHz and $\Omega_5 = 119.5$ kHz for Al wire. The first bending mode is not seen because it has been buckled due to the a/l ratio exceeding the critical rise.

2.2   Model for Out-of-Plane Vibration

The first natural frequency determined in the modal analysis of the wires is in out-of-plane bending mode. It is well known that most of the energy goes into the first mode. Thus, it is very important to calculate eigenvalues of out-of-plane bending modes for the wires. To calculate the eigenvalues for out-of-plane bending modes, the wire is assumed to be a straight beam from top view and modeled using the Euler-Bernoulli beam theory. Figure 2.3 shows the schematic of the wire modeled for out-of-plane vibration. it should be noted that L is span length of the wire.
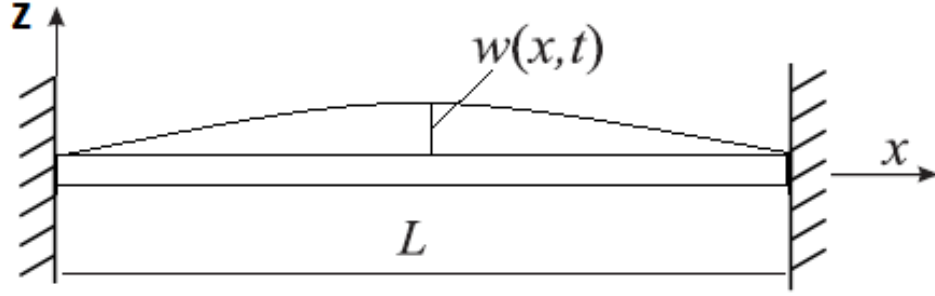
Figure 2.3: The modeled wire for out-of-plane vibration from top view

For a fixed-fixed straight beam free of transverse loads, we can write its equation of motion as [36]

$$\rho A \frac{\partial^2 w}{\partial t^2} + EI \frac{\partial^4 w}{\partial x^4} - N \frac{\partial^2 w}{\partial x^2} = 0 \tag{2.25}$$

where $w(x,t)$ is a component of the displacement field along the z direction. Substitute in the equation of motion with the harmonic solution form

$$w(x,t) = \phi(x)e^{i\omega t}$$

$$EI \frac{\partial^4 \phi}{\partial x^4} - N \frac{\partial^2 \phi}{\partial x^2} - \rho A w^2 \phi = 0 \tag{2.26}$$

Substituting the exponential solution form $\phi(x) = e^{\beta x}$ and we obtain

$$EI\beta^4 - N\beta^2 - \rho A w^2 = 0 \tag{2.27}$$

$$\beta_1^2 = \phi + \sqrt{\phi^2 + \frac{w^2}{w_{fr}^2}} , \quad \beta_2^2 = \phi - \sqrt{\phi^2 + \frac{w^2}{w_{fr}^2}} \tag{2.28}$$

where

$$\phi = \frac{N}{2EI}, \quad w_{fr}^2 = \frac{EI}{\rho A} \tag{2.29}$$

The general solution of this problem is:

$$\phi(x) = C_1 cos(\beta_1 x) + C_2 sin(\beta_1 x) + C_3 cosh(\beta_2 x) + C_4 sinh(\beta_2 x) \tag{2.30}$$

Applying the boundary conditions, Eq. (2.21), to Eq. (2.30) gives four equations for the constants $C_1 - C_4$. Figure 2.4 depicts the first six out-of-plane bending modes for the wires or in-plane bending modes for a fixed-fixed straight beam.
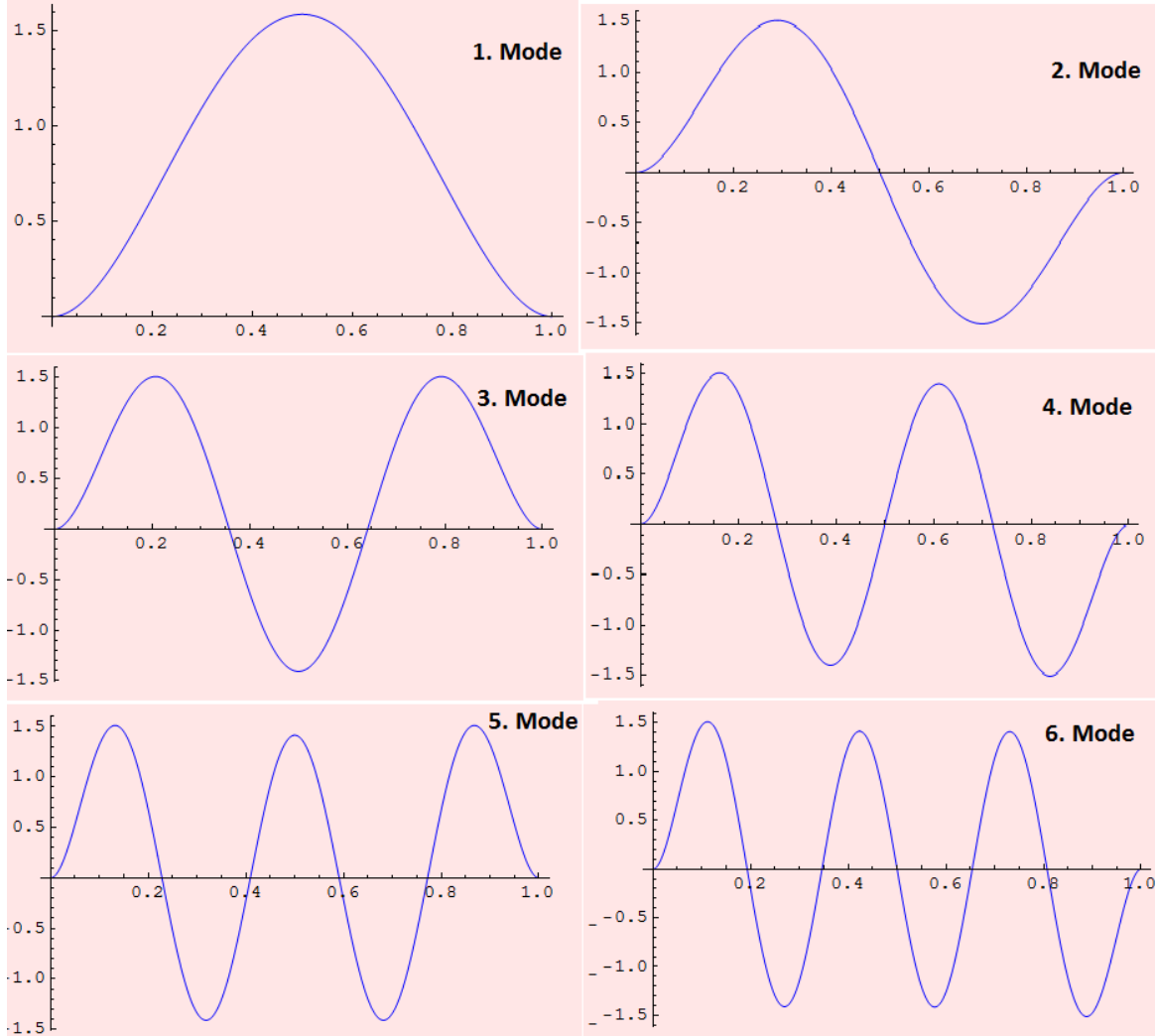
Figure 2.4: First six out-of-plane modes for the wires or in-plane modes for a fixed-fixed straight beam.

.

It is found that the first, second, third, fourth and fifth bending modes appear at $\Omega_1 = 4.8$ kHz, $\Omega_2 = 13.1$ kHz, $\Omega_3 = 25.6$ kHz, $\Omega_4 = 42.2$ kHz and $\Omega_5 = 63$ kHz for Al wire, respectively. The results obtained from analytical model are in good agreement with FEA and experiments.

2.3 Thermal Model

Evaluating the temperature distribution along the bonding wire is necessary to obtain the thermal strain / load. Thus, a partial differential equation describing temperature distribution along the wire over time is introduced and analyzed as [37]

$$k\left(\frac{\partial^2 T}{\partial x^2} + \frac{\partial^2 T}{\partial y^2} + \frac{\partial^2 T}{\partial z^2}\right) + P - \frac{hP_e}{A}(T - T_a) = \rho C_p \frac{\partial T}{\partial t} \tag{2.31}$$

where k, is thermal conductivity coefficient, P is the power input due to externally applied current, P_e is circumference of the wire, h is heat convection coefficient, T_a is ambient temperature, and C_p is heat capacity of the wire. Input power is given by

$$P = R_e \frac{I^2}{A^2} \tag{2.32}$$

where R_e is electrical resistivity of the material and I is current passing through the wire.

We assume steady state conditions and that heat conduction occurs only in x-direction, that is

$$\frac{\partial T}{\partial y} = 0, \quad \frac{\partial T}{\partial z} = 0, \quad \text{and} \quad \frac{\partial T}{\partial t} = 0 \tag{2.33}$$

Substituting with these relations into Eq.(2.31) yields;

$$k\frac{\partial^2 T}{\partial x^2} + R_e \frac{I^2}{A^2} - \frac{hP_e}{A}(T - T_a) = 0 \tag{2.34}$$

which can be simplified to

$$T^{''} - aT = -b \tag{2.35}$$

where $a = \frac{hP_e}{Ak}$, $b = R_e \frac{I^2}{kA^2} + \frac{hP_e T_a}{kA}$

General solution can be written as

$$T(x) = c_1 e^{\sqrt{a}x} + c_2 e^{-\sqrt{a}x} + \frac{b}{a} \tag{2.36}$$

Applying the boundary conditions;

$$T(0) = T(L) = T_e, \quad T'(\frac{l}{2}) = 0 \tag{2.37}$$

where T_e can be obtained from experimental measurements, and $T'(\frac{l}{2})$ is zero in the middle of the wire due to wire geometrical symmetry. Applying only two of the boundary conditions listed in Eq. (2.37) is adequate to obtain the general solution Eq. (2.36). The temperature distribution along an Al wire ($l = 11$ mm, $a = 4$ mm and $d = 300\mu m$) carrying a current of ($I = 2$ A) is shown in Figure 2.5. The boundary conditions have been set based on experimentally measured data (20 $^\circ C$).
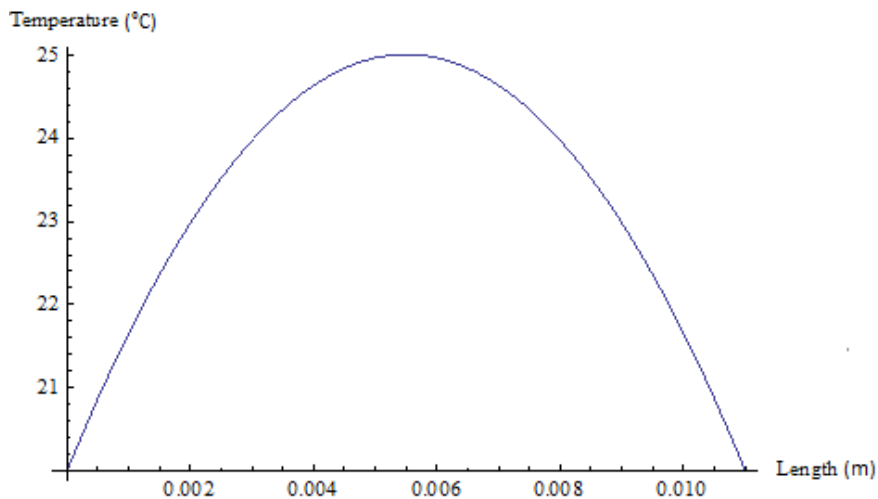
Figure 2.5: Temperature distribution along Al wire

2.4 FEA Model

In addition, finite element model was developed for steady-state analysis of the displacement and temperature distribution under DC current, and modal analysis of bonding wires. First, a picture of the wire was taken to-scale and imported into SolidWorks to draw a model of the tested specimen. Then it was imported to Comsol for static and dynamic analysis. Three different analysis types were needed

for static analysis in Comsol: 1- Solid, Stress-Strain type Figure, 2- Conductive Media DC and 3- General Heat Transfer. Thermal boundary conditions for those types are: boundaries are fixed-fixed, ground-Power input (as DC current) and all sub-domain is heat flux respectively.
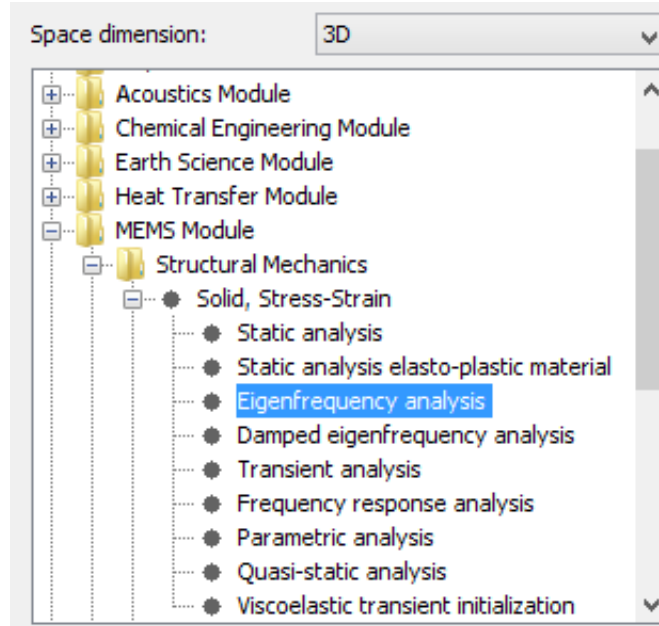
Figure 2.6: Analysis types in Comsol

An analysis type was adequate to obtain undamped eigenfrequencies and mode shapes for the wire. Figure 2.6 depicts a analysis types for obtaining eigenfrequencies in Comsol. Mechanical boundary conditions was set to fixed-fixed. The material properties of the wire given in Table 3.1 was also applied to model in Comsol. Figure 2.7 shows the 3D of model of the wire used in experiments. The wire was then discretized into points in order to export the simulated displacement results and compare them with experimental results. Figure 2.8 shows the wire with discretization points.

In order to save on time and computer storage, mesh size was set to normal throughout simulation. Complete mesh consists of 1377 elements, number of degrees of freedom solved for is 8859 and solution time is 56 s. The results of static and dynamic analysis are presented in chapter 4.
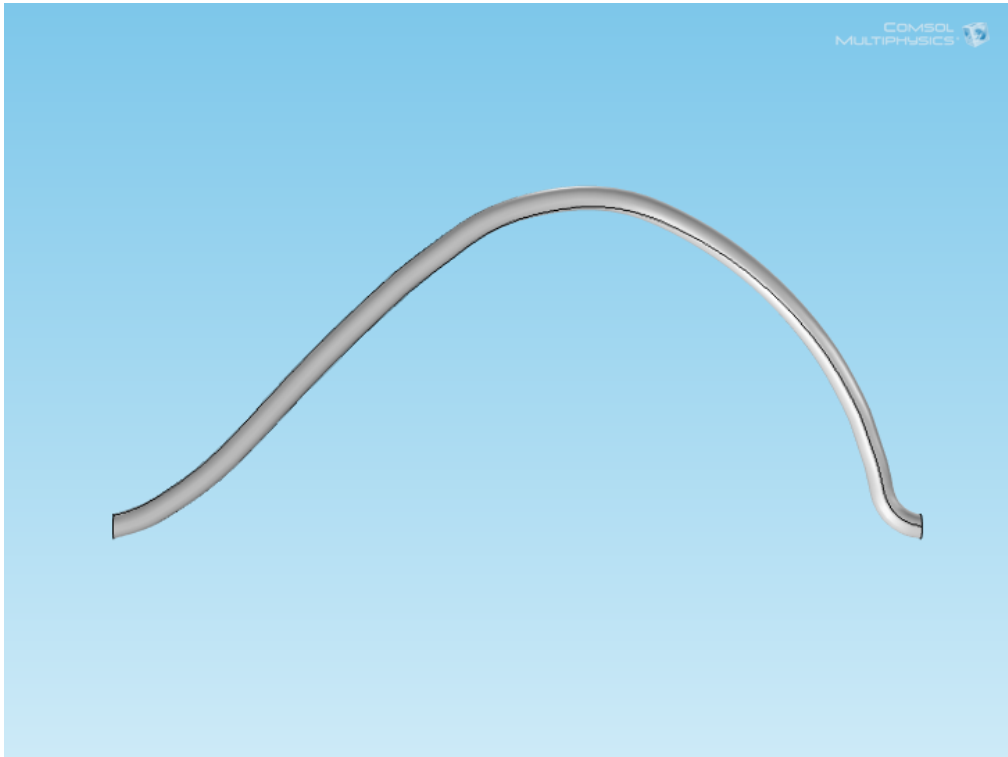
Figure 2.7: Model of the wire in Comsol
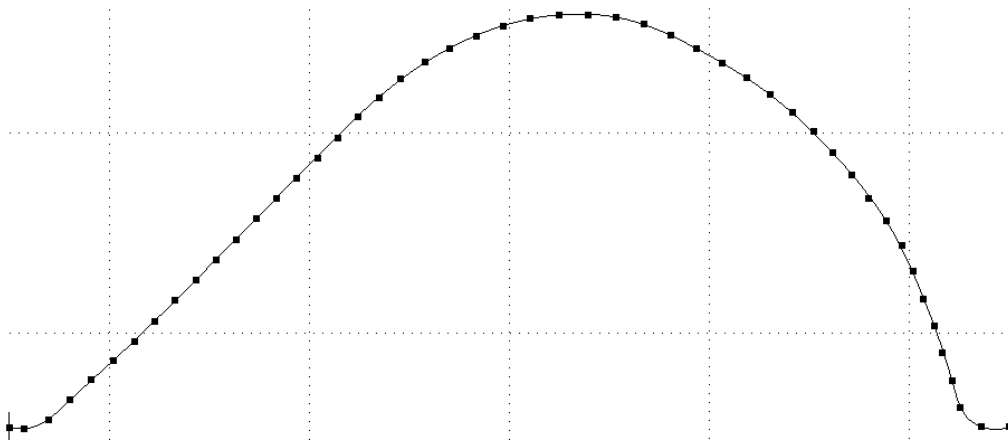
Figure 2.8: Model with discretization points superimposed

Chapter 3

Experimental Setup

Joule heating causing temperature rise in bonding wires, also causes compressive stresses due to the wire tendency to expand. This imposes a limit on the maximum deflection and temperature that the wire can withstand before failure. In addition, estimating the wire resonant frequencies is critical to determine the safe operating conditions for the wire.

In this chapter, experimental techniques to analyze the quasi-static and dynamic response of bonding wires are developed and presented. First, an experimental technique is developed to measure quasi-static displacement of bonding wire. It is then deployed to measure the displacement, as well as peak temperature, of Al, Cu and CuCorAl bonding wires under DC current. Second, we developed two experimental techniques for dynamic wire analysis: an impact (hammer-style) technique to obtain the natural frequencies of the wire and harmonic excitation technique to obtain frequency response of the wires.

3.1 Specimen Preparation

Wires were bonded to Direct Copper bonded (DCB) substrate, Figure 3.1, to connect to identical copper films. The DCB substrates, Tianjin Century Electronics Co., are made of copper layers 300 μm fused to ceramic substrate at high temperature [38]. The bonding process, Heraeus Company, involves an ultrasonic

bonding[39].
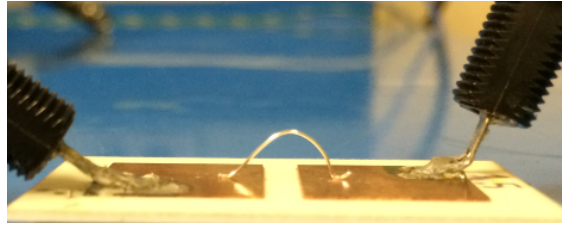
Figure 3.1: Tested wire on DCB Substrate.

An SEM picture of an etched CuCorAl wire, Figure 3.2, show that the Al coat is 25μm thick [6].
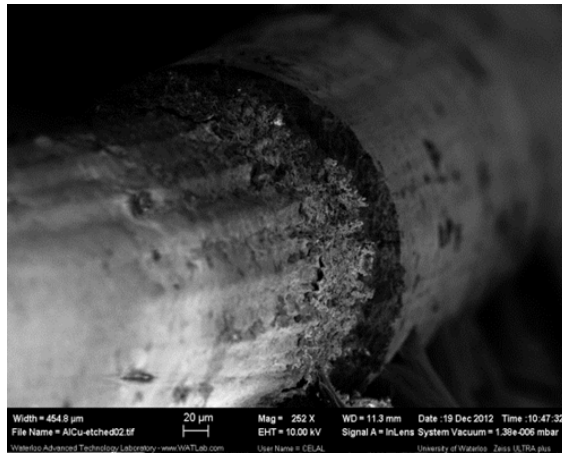
Figure 3.2: Etched CuCorAl wire

Table 3.1: Material properties of the wire specimen

Material	Aluminum	Copper	Aluminum coated Copper
λ (W/mK)	237	401	400
ρ (kg m^3)	2700	8980	8700
E (Gpa)	69	130	120
v	0.35	0.343	0.35
ρ_r ($\mu\Omega$.cm)	2.8	1.68	1.72
$\alpha(\times 10^{-6})$/K	23.1	17	17

Table 3.1 lists the material properties of the tested wire specimens where λ is thermal conductivity, v is Poisson's ratio, ρ_r is electrical resistivity at $20°C$. The dimensions of the wire specimen employed in the static and dynamic analyses are listed in Tables 3.2 and 3.3, respectively. The gross diameter of CuCorAl wire is 300 μm, where the Cu core diameter is 250 μm and the Al coating is 25 μm thick.

Table 3.2: Dimensions of tested the wires for static analysis

Material	Aluminum	Copper	Aluminum coated Copper
l (mm)	11	11	11
a (mm)	4	4	4
d (μm)	300	300	300

Table 3.3: Dimensions of tested the wires for dynamic analysis

Material	Aluminum	Aluminum coated Copper
l (mm)	11	10
a (mm)	4	4
d (μm)	300	300

3.2 Quasi-Static Analysis

Substrate of Al thick wire was taped on vibrometer table and wired to DC power supply. A laser vibrometer was used to measure the displacement signal of the wire. Since, the laser vibrometer only measures motions in plane direction or time varying responses, the displacement-response of the wires was obtained by applying a current pulse train, Figure 3.3 to the wires. A probe were soldered to each of the copper patches on the DCB substrate, Figure 3.1, and used to pass the current through bonding wire. The displacement of the wire peak point was measured as a

function of time using the LDV. The pulse width was set to $PW = 2$–3 s while the pulse amplitude was varied. Furthermore, the bead of a thermocouple was attached to middle of wire bonding using kapton tape to measure peak temperature under various DC currents. Results are shown in chapter 4.
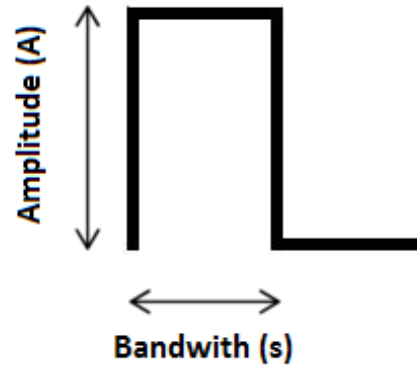
Figure 3.3: Schematic of pulse DC used in experiment

This experiment was developed to determine the thermal time constant (rise and fall times) of the wire, their transient response to step excitation, and their static displacement under DC current. Figure 3.4 demonstrates experimental setup for quasi-static analysis.
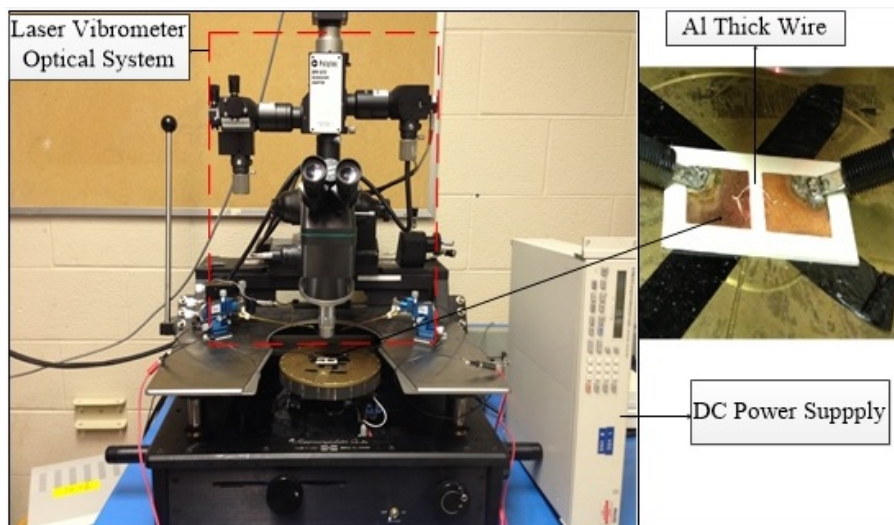
Figure 3.4: Experimental setup for static analysis

3.3   Dynamic Analysis

3.3.1   Modal Analysis

An impact experiment was designed to obtain the modal response of bonding wires. An Al block was attached to one end of the DCB substrate. The substrate and a solenoid actuator were attached to the stage of a probe station, figure 3.6, such that the block and the solenoid plunger were aligned.
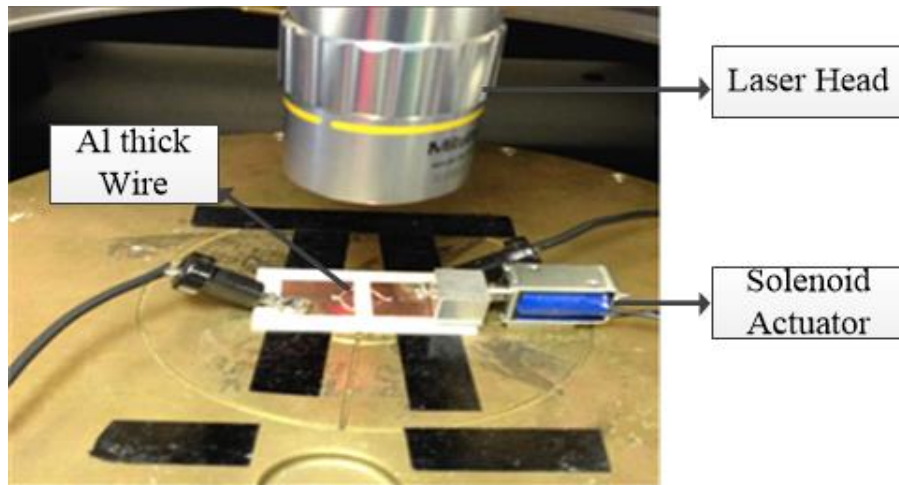
Figure 3.5: Experimental setup for natural frequency analysis

The actuator was used to deliver low frequency impacts to the block, thereby delivering an impact (pulse) train to the bonding wire.
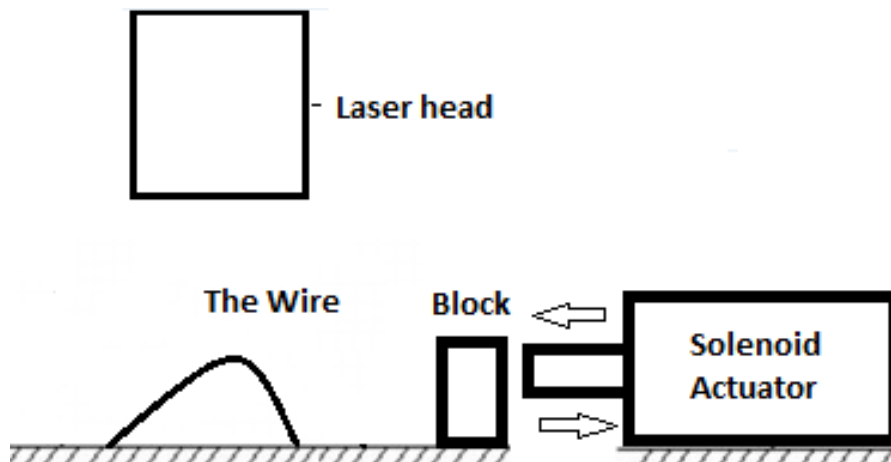
Figure 3.6: Schematic of experimental using solenoid actuator

A function generator was used to drive the solenoid actuator and command the frequency ($f_p = 10\ Hz$) and duty cycle ($D = 0.2$) of the impact pulse train. Advantage of using this technique is that natural frequencies of the wire are measured without any loading. Figure 3.5 shows the a schematic of experimental setup used for obtaining the natural frequencies of bonding wires. The vibrometer also gives the FFT of the measured velocity. Under these experimental conditions, the DC current further was applied to the wire, and thus its axial compressive load, was varied in order to analyze the effect of thermal load on the natural frequencies of the wires.

3.3.2 Harmonic Atuator

Moreover, a technique for harmonic actuation was developed to obtain the frequency-response curves and mode shapes of bonding wire. Voltage to current amplifier circuit was used for thermal excitation of the wires. A function generator supplies the AC current. A power source supplied bias (DC) current. An amplifier circuit (Voltage to Current Converter), schematic of which is shown in Figure 3.7, amplifies the AC current.
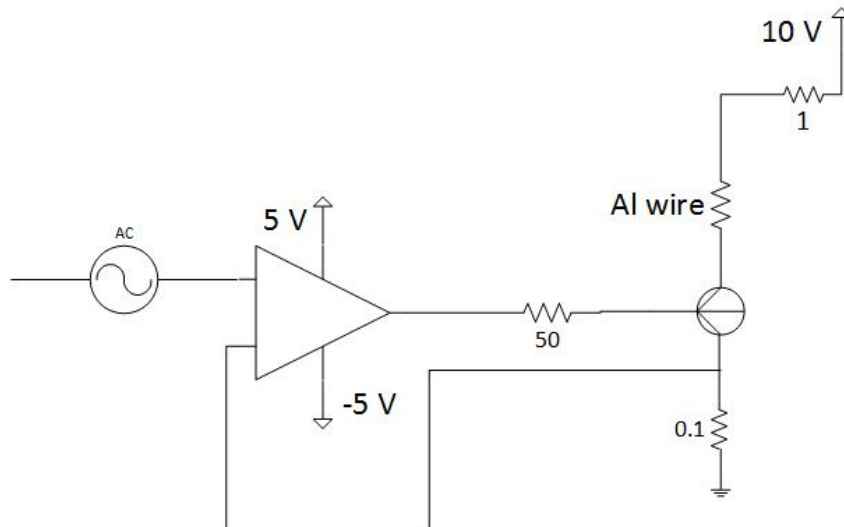
Figure 3.7: Schematic of circuit used for modal analysis

Figure 3.8 shows the excitation circuit and the wire under laser vibrometer. To

determine a mode shape, the excitation frequency was held constant at the natural frequency corresponding to the mode shape as determined via modal analysis. The amplitude of the current was held constant at: $A_{AC} = 3.4$ A and $A_{DC} = 2.2$ A. The scanning mode of the Laser vibrometer was used to obtain the mode shape of the wire. In this mode, the Laser vibrometer scans a two-dimensional point-grid defined on a given structure to measure the velocity at each point.
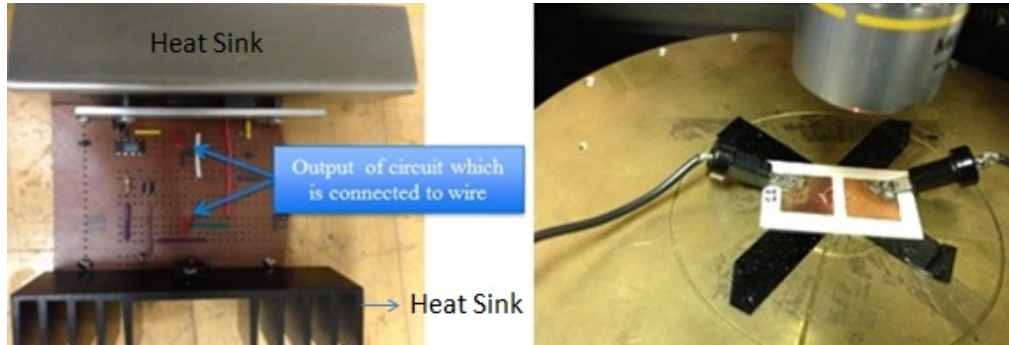
Figure 3.8: Harmonic actuation circuit and wire setup

Since the field of view of the standard 10X microscope objective is less than 2 mm, while the wire specimen is 10 mm long (span length is 13.75mm), multiple scanning events had to be stitched together to cover the wire span. It was found that curvature of the wire further reduced the scanning field to 0.570 mm. As a result, the number of scan events required for a 10 mm long wire was 50 to obtain out-of-plane modes. Experimental setup for obtaining out-of-plane bending modes is shown in Figure 3.9
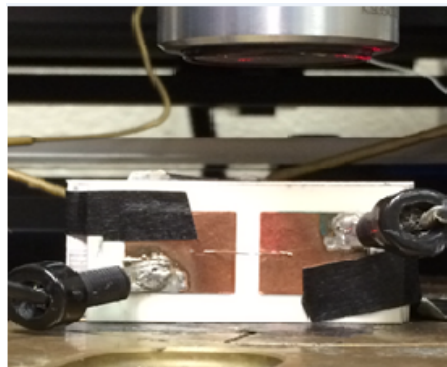
Figure 3.9: Experimental setup for out-of-plane bending mode shapes

The point-grids comprising a scan event for each of out-of-plane bending the mode shapes are listed in Table 3.4. First and second out-of-plane bending modes are obtained using this method.

Table 3.4:   Point-grids used to obtain the mode shapes

Bending Mode	Grid points
First out-of-plane	30×5
Second out-of-plane	18×5

Experimental setup for obtaining out-of-plane bending modes is shown in Figure 3.10 On the other hand, for in-plane bending modes, it was found that as the scan approaches the edges of the field of view, the reflected laser beam lies outside the angular aperture of the microscope objective due to wire curvature. Thus we needed to design a rotary stage to align reflection of laser beam. Then, we experimentally measured nodes along the wire while the wire is resonating at first, second, and third in-plane bending modes. Experimental results are compared with simulation results in chapter 4.
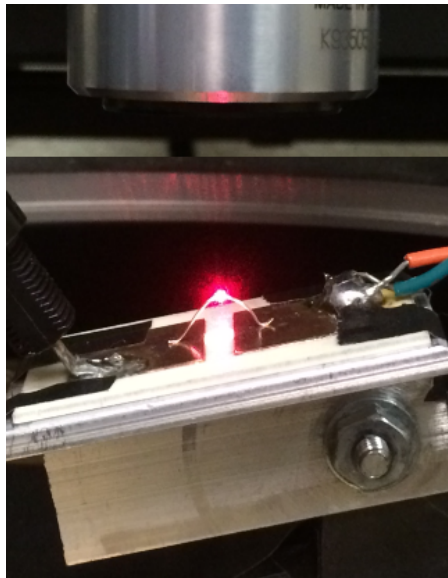
Figure 3.10: Experimental setup for in-plane bending mode shapes

Chapter 4

Results

In this chapter, static and dynamic results obtained from experiments and FEA analysis are presented and compared to each other. Static results are vital to determine the thermal loading conditions on the wire. Dynamic results are more critical, in terms of reliability, since operating the system close to resonant frequencies causes high deflections which also leads to high stresses on wire heels. This may eventually result in early failure at a lower number of power cycles. For example, Barber et al. [40] reported that bonding wires failed when they resonate under low current thermal actuation after a couple of minutes. Thus, obtaining the resonant frequencies and mode shapes is desirable in order to avoid early failure in IGBT modules.

4.1 Static Results

4.1.1 Experimental

The temperature of 11 mm long Al, Cu, and CuCorAl wires were experimentally measured at wire peak using a thermocouple. The experimental results, Figure 4.1, show that the Al wire has higher peak temperature than CuCorAl, which in turn has a higher temperature than Cu. The temperature increase in proportion to the Al content of the wire is expected due to Al high resistivity and lower conductivity
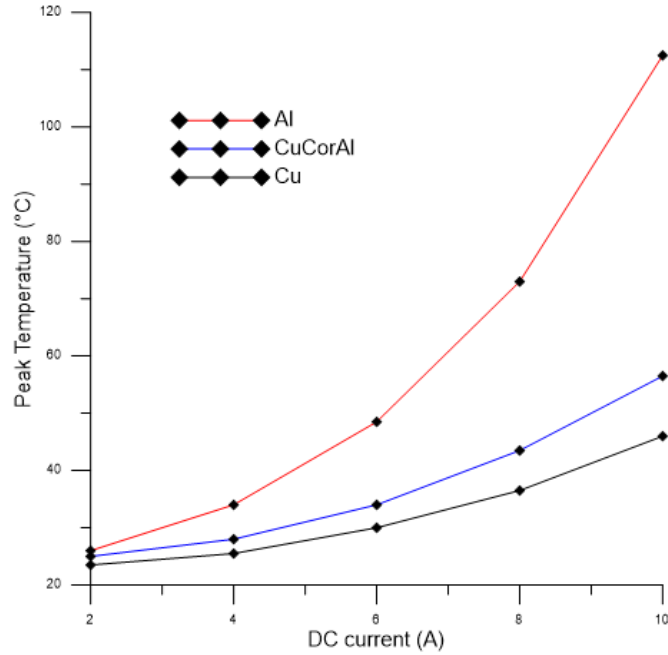
Figure 4.1: Peak temperature of 11 mm long Al, CuCorAl, and Cu wires with DC current

compared to Cu. This is not desirable in bonding wires because high temperature leads high stresses in wire heels and reduces the wire fatigue endurance. Thus, Cu and CuCorAl wires are more promising due to their lower resistivity and higher conductivity.
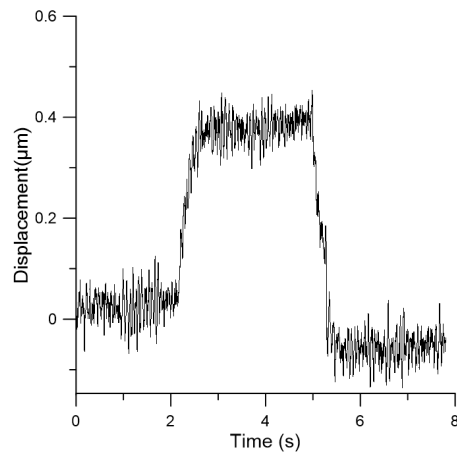
Figure 4.2: Response of Al wire to a current pulse with amplitude 2 A and $PW = 2.6$ s

Furthermore, the maximum wire displacement, at the peak point, was measured.

Figure 4.2 shows the peak point displacement of Al wire as a function of time in response to a current pulse with an amplitude of 2 A and pulse width $PW = 2.5$ s.

It can be seen from Figure 4.2 that power supply was off for about two seconds then it was turned on for 2.5 s then reset to OFF state. The PW was set to a value significantly larger than the rise time of the wire to allow it to settle down, and obtain a quasi-static response approximating the steady-state response of the wire to DC current equal to that of the pulse amplitude. The figure shows that the Al wire reaches 0.4 μ m (95 % of steady-state displacement) in $3\tau \approx 0.57$ s corresponding to a rise time of $\tau = 0.19$ s, then the wire comes back to initial shape when the power is turned off. The difference between the initial and final OFF displacement levels is due to drift over time in the vibrometer displacement measurements.
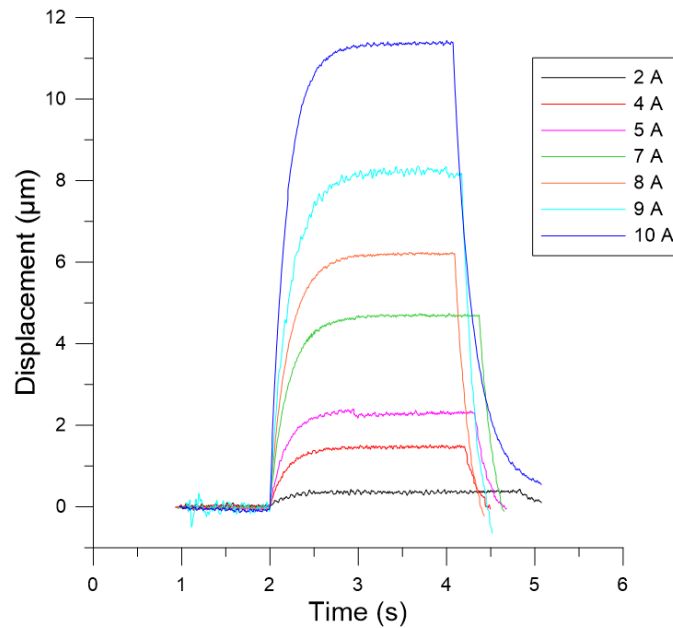
Figure 4.3: Displacement of Al wire peak point as a function of time for pulse amplitudes from 2 A to 10 A

Table 4.1: Time constants for Al wire

Current	Rise Time	Fall Time
2 A	0.2285	0.0859
4 A	0.1904	0.0664
5 A	0.1855	0.0654
7 A	0.2031	0.0605
8 A	0.2070	0.0605
9 A	0.2207	0.0595
10 A	0.1914	0.1064
Mean:	0.2038	0.0721
St. Dev:	0.0161	0.0176

Figure 4.3 depicts the peak point displacement of Al wire under current pulses with amplitudes of 2, 4, 5, 7, 8, 9, and 10 A and pulse width in the range PW=2–4.5 s. The steady-state wire displacement under 2 A and 10 A pulse DC current is measured as 0.4 nm and 11.4 μm, respectively. The noise floor is measured as the standard deviation of the displacement signal over xx s when the current pulse is in OFF state. It was found to be 10 nm. The rise time and fall time for all Al wire loading cases are listed in 4.1. Their mean and standard deviation were found to be 0.20 ± 0.016 s for the rise time and 0.07 ± 0.017 s for the fall time.
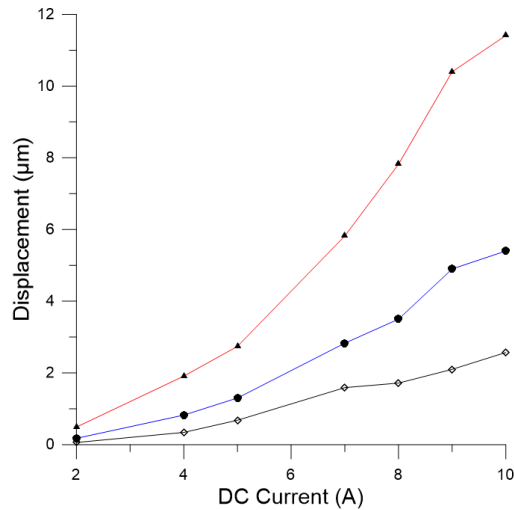
Figure 4.4: Steady-state displacement of the peak point for Al, CuCorAl, and Cu wires as a function of DC current

Using same technique, the time-history of peak point displacement for Cu and CuCorAl wires were obtained under pulse current with amplitudes 2, 4, 5, 7, 8, 9, and 10 A and pulse width in the range PW=2.5–4.5 s. The relationships between steady-state displacement and DC current for all three wire types are shown in Figure 4.4. It is noted that Al wire undergoes larger displacements, and therefore larger strains and stresses, which results in less fatigue endurance, than CuCorAl wire which are in turn more prone to fatigue than Cu wire.

4.1.2   Finite Element Method
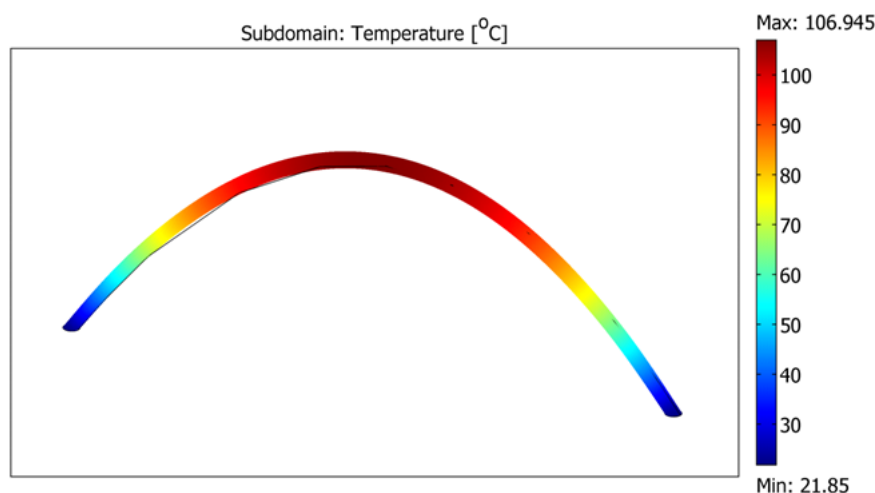
Figure 4.5: Temperature distribution along 11 mm Al wire under 10 A DC current

Finite element method using Comsol is implemented to obtain temperature distribution along the wire and verify existing the maximum temperature obtained from experimental results. For instance, Figure 4.5 shows temperature distribution along Al wire under 10 A.

Based on Figure 4.5, a maximum temperature of 106 $°C$ occurs in the peak point of the Al wire under 10 A DC current. However, maximum stress was observed on theel of the wires Temperature on the heel was measured as 21$°C$ for 10 A DC current. This simulation was implemented for the Al and Cu wires for currents varying from 2 A to 10 A. The maximum temperatures in the wires are compared to experimental results in Figure 4.6 and Figure 4.7. Simulation and experimental
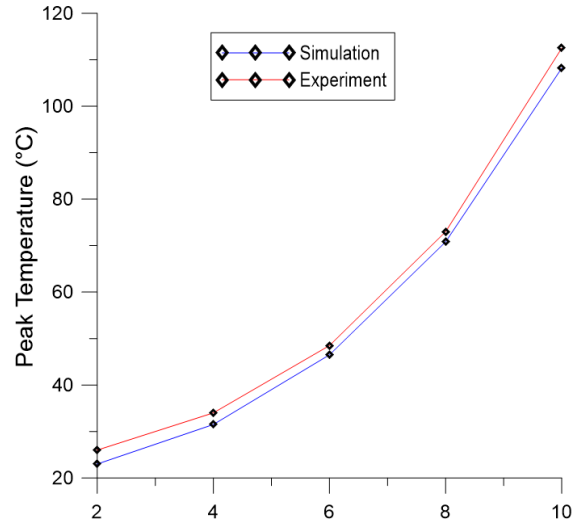
Figure 4.6: Temperature at the peak point of 11 mm Al wire as a function DC current

results are in very good agreement. Material properties of the wire used in Comsol is given in Table 3.1.
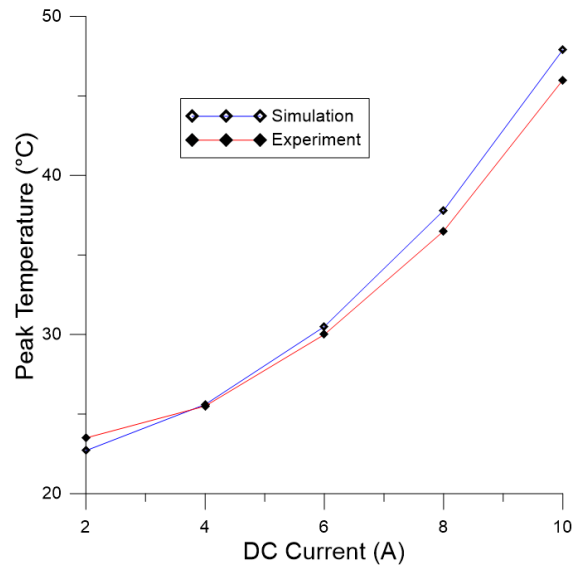
Figure 4.7: Temperature at the peak point of 11 mm Cu wire as a function DC current

4.2 Modal analysis

4.3 Experimental Modal analysis

Firstly, as it is mentioned before, obtaining natural frequencies of the wires is vital to operate system in safe conditions. In the developed hammer-type(solenoid actuation) excitation technique, the substrate of the Al wire was excited by a solenoid actuator to determine the wire natural frequencies without thermal load. Even thoug laser vibrometer only measures in-plane motions, due to circular cross section of the wire, it also measures out-of-plane motions. The laser vibrometer was used to read velocity response of the wires. Figure 4.8 demonstrates the first five natural frequencies of the Al wire. Natural frequencies of 11 mm long Al wire below 40 kHz appear at f_1= 5.7 kHz, f_2= 14.7 kHz, f_3= 17 kHz, f_4= 33 kHz, and f_5= 34 kHz.
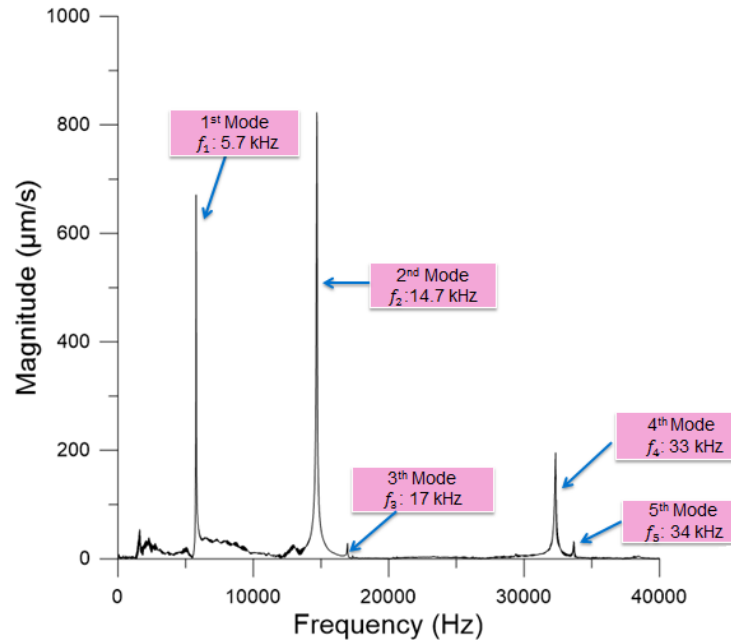
Figure 4.8: FFT of Al wire using solenoid actuator

Also, Figure 4.9 shows velocity response of CuCorAl wire using solenoid actuator without load. The third mode has very small magnitude in Figures 4.8 and 4.9. The reason is that first, since the laser beam shines around the midpoint of the

wire where a node exists, around which the deflection is very small. Further, the wire shape differs from one specimen to the other which changes the position of the node in each specimen. Natural frequencies of 10 mm long CuCorAl wire below 30 kHz appear at f_1= 4.1 kHz, f_2= 11.8 kHz, f_3= 13.1 kHz, f_4= 25.2 kHz, and f_5= 25.8 kHz.
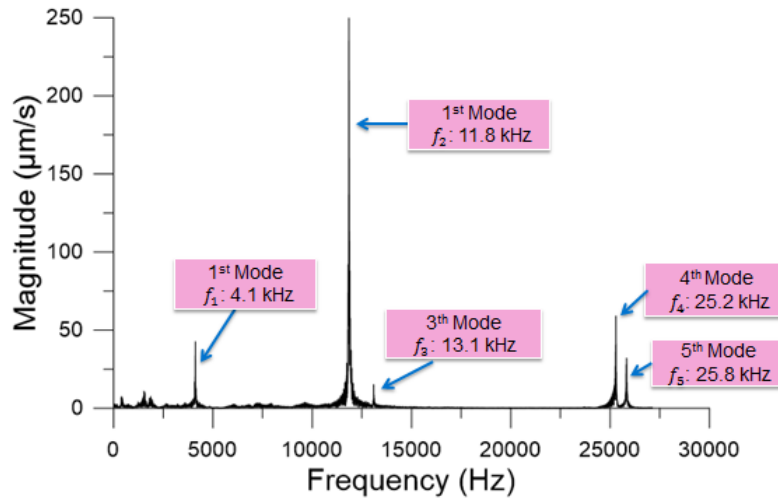
Figure 4.9: FFT of CuCorAl wire using solenoid actuator

After exciting the wire using the solenoid actuator, the time history of the velocity of CuCoral wire was measured and depicted in Figure 4.10.
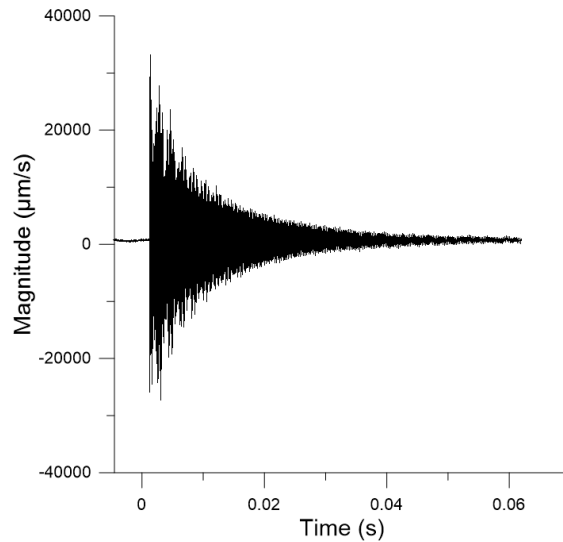
Figure 4.10: Time response of CuCorAl wire using solenoid actuator

41

4.3.1 FE Eigenvalue Analysis

To verify the natural frequencies obtained experimentally and to identify the visualize the mode shapes corresponding to them, modal analysis using the FEM was carried out. The first six mode shapes of 10 mm long CuCorAl were obtained and are presented in Figure 4.11.
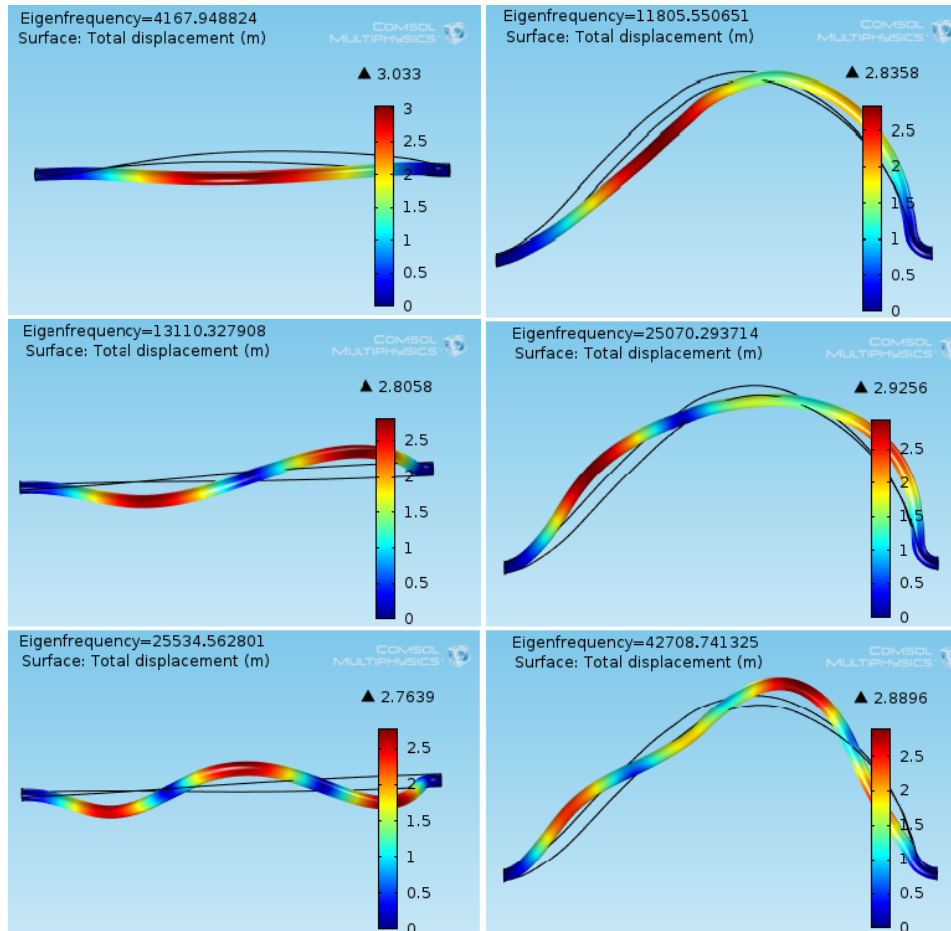
Figure 4.11: Mode shapes of 10 mm long CuCorAl wire

The left column of the figure shows top views of modes 1, 3, and 5, which are the first, second, and third out-of-plane bending modes of the wire. The right column of the figure shows front views of modes 2, 4, and 6, which are the second, third, and fourth in-plane bending modes of the wire. The natural frequencies of those modes are 4.1 kHz, 11.8 kHz, 13.1 kHz, 25.07 kHz, and 25.5 kHz in FEA model. The natural frequencies of the first five modes are in close agreement with the five

experimentally measured natural frequencies of CuCorAl wire.

4.4 Effect of Thermal Loads on Natural Frequencies

Since bonding wires might be exposed to high electric power, this will have an effect on their natural frequencies and thus their response. If there is a huge drop in natural frequency of the wire, the drop may drive the wire to resonate and fail at lower power cycles. Therefore, we analyzed the Al and CuCorAl wires natural frequencies as function of DC current.

Figure 4.12 shows the drop in natural frequency of the second in-plane bending mode of Al-wire as a function of DC current.
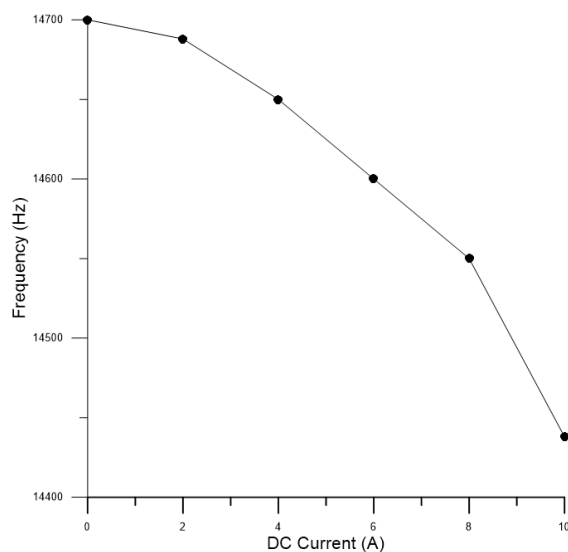
Figure 4.12: The natural frequency of Al-wire second in-plane bending mode as a function of DC current

Figure 4.12 shows that the drop in natural frequency versus DC current is insignificant. The measured natural frequency at zero DC current was 14.7 kHz and it decreases to 14.438 kHz at 10 A indicating a change of 0.26 kHz for 10 A increase in DC current.

Figure 4.13 shows the drop in natural frequency for four modes vibration modes

43
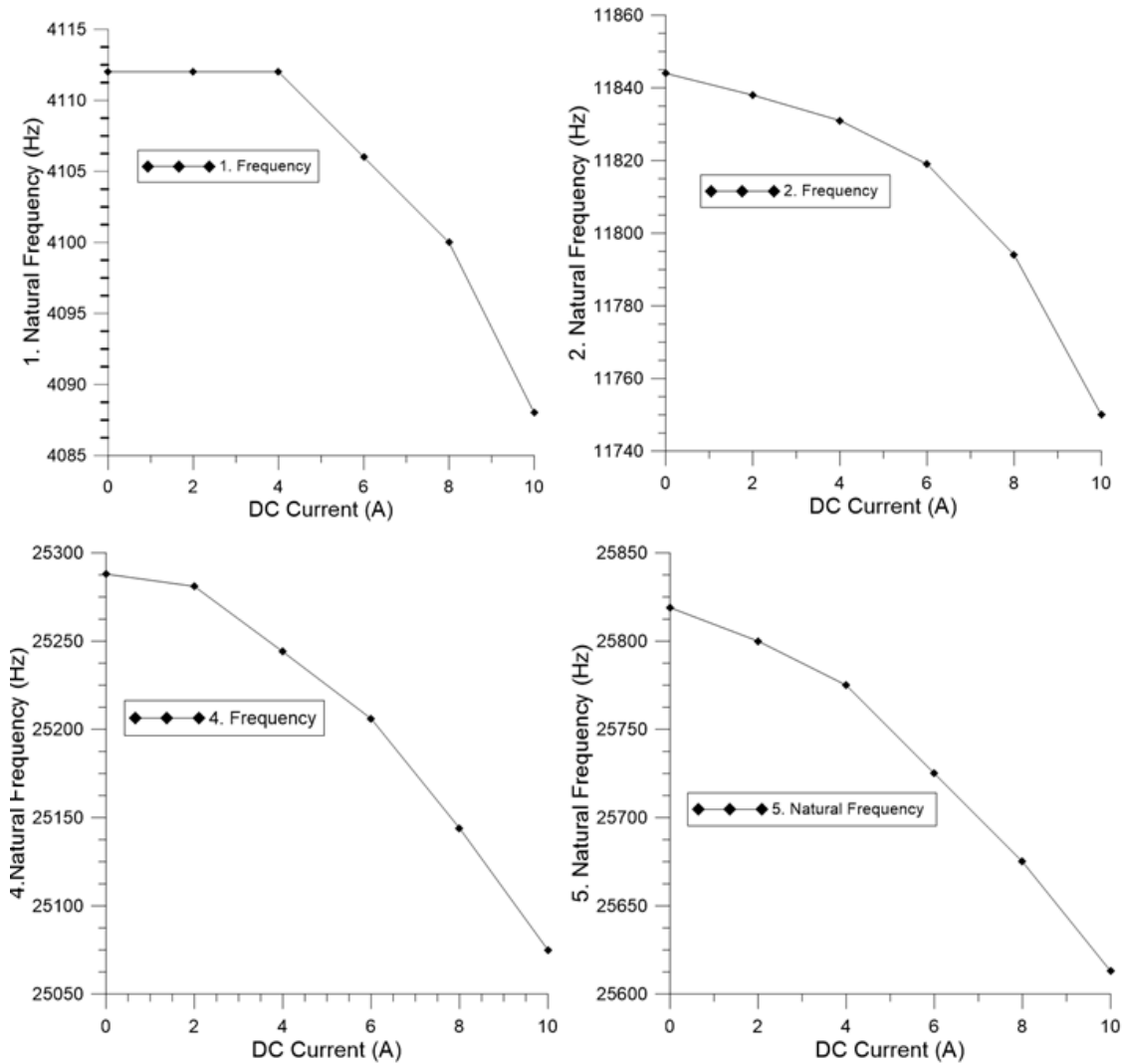
Figure 4.13: The natural frequencies of CuCorAl-wire as a function of DC current

of CuCorAl wire as a function of DC current. The drop at natural frequencies of CuCorAl wire under 10 DC current thermal load, f_1, f_2, f_4, and f_5 was measured as 24 Hz, 94 Hz, 213 Hz, and 206 Hz respectively. The measured the drop results shows that the effect of thermal load on the Al and CucorAl wires natural frequencies is minimal for the four modes measured, implying that the wire keeps its mechanical integrity over a wide range of thermal loading conditions. In Figure 4.13, we note that the drop in natural frequency for the first mode is less than 1 Hz with increase in DC current up to 4 A. We were unable to measure this drop due to restrictions on the minimum resolution of laser vibrometer (1 Hz).

If we compare Figure 4.12 with Figure 4.13 for the second vibration mode, the drop in the second natural frequency of the Al wire is (260 Hz), higher than the drop in second natural frequency of CuCorAl (94 Hz) under 10 A DC current. This points out that CucorAl wires are more reliable than Al wires in terms of their dynamic response.

4.5   Harmonic analysis

Harmonic actuation technique is developed to measure frequency response curves and to estimate the quality factor of the wire n^{th} mode shape using the half-power bandwidth method. Where n^{th} is the number of the mode shape.

Furthermore, the technique is used to verify the natural frequency results obtained from modal analysis. For instance, Figure 4.14 shows the maximum velocity response of the CuCorAl wire resonating at the fifth mode. If we compare Figure 4.14 with 4.9, the response for the fifth mode matches exactly, which proves the accuracy of both thermal actuator and hammer-type excitation techniques for identifying natural frequencies of the wires.
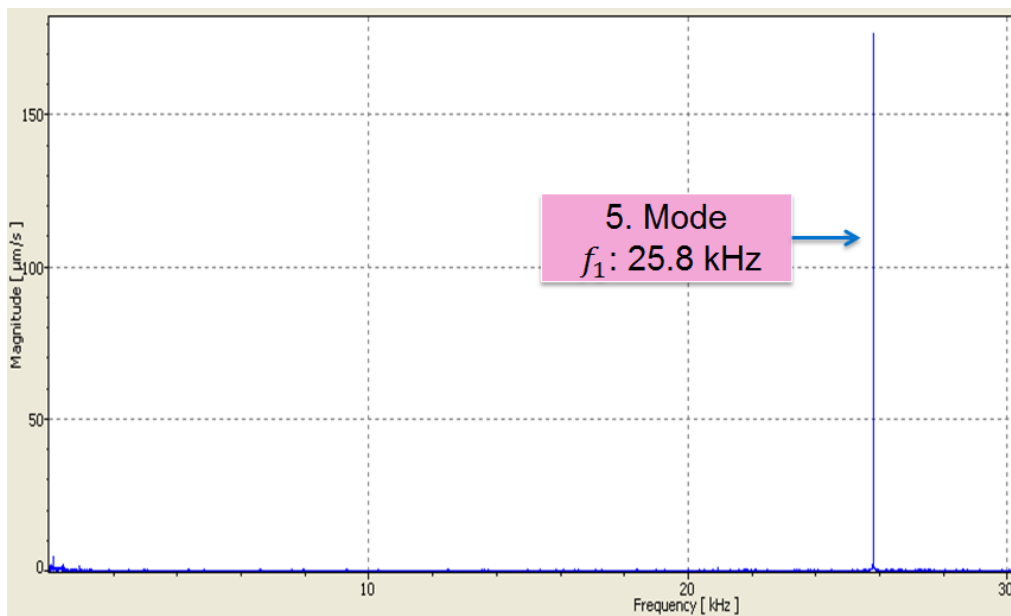
Figure 4.14: FFT of CuCorAl wire using thermal actuator

4.5.1 Mode Shapes

In addition, we used harmonic actuation technique to measure specifically mode shapes of the CuCorAl wire. Figure 4.15 shows a measured scan event described on the wire. Velocity responses were measured for each scan event and stitched together with others to obtain full out-of-plane bending modes of the wire.
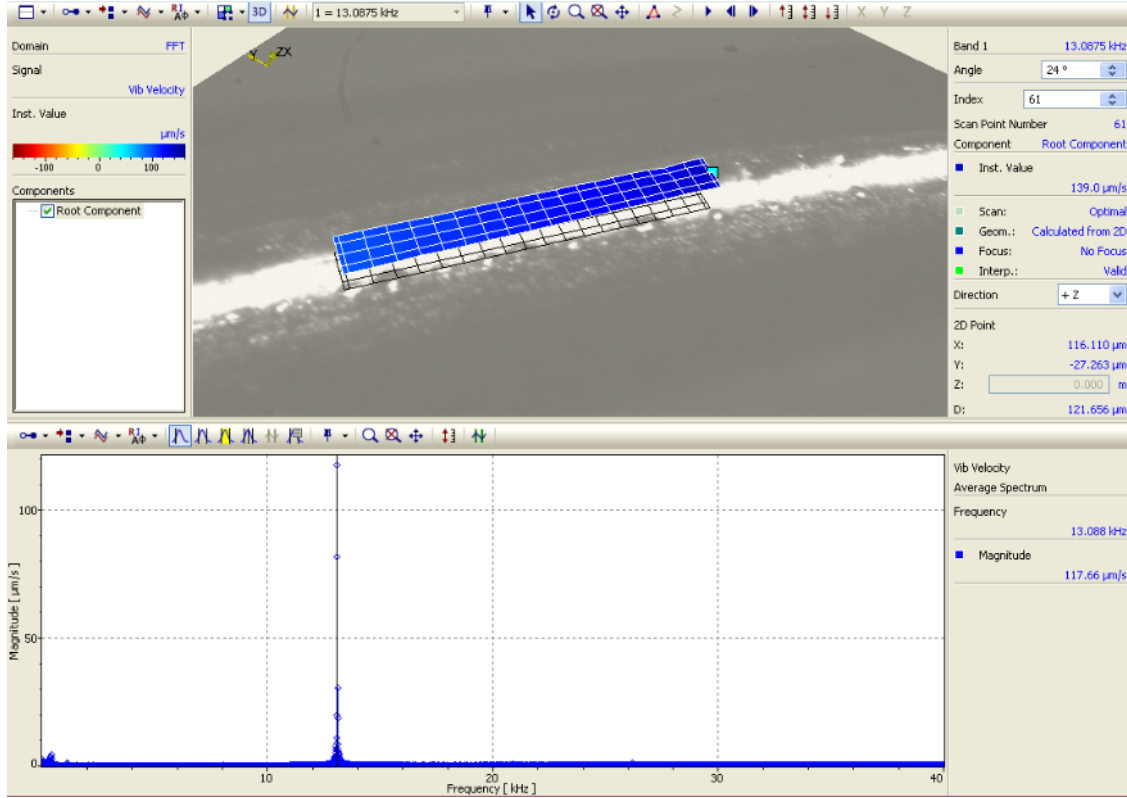
Figure 4.15: a scan event on the wire

While the wire excited at first out-of-plane bending mode ($\Omega_1 = 4.1\ kHz$) using harmonic actuator, first and second out-of-plane bending mode shape of the wire were experimentally measured for each scan event. After scanning whole span of the wire, scanning events are stitched together to obtain full mode shapes of the wire. Further, experimental results are compared with FEA results. Figures 4.16 and 4.17 and show comparison of experimental and FEA results for first and second out-of-plane bending modes from top view of the wire respectively . The results are in good agreement.

For in-plane bending mode shapes, nodes along the wire for second, third, and
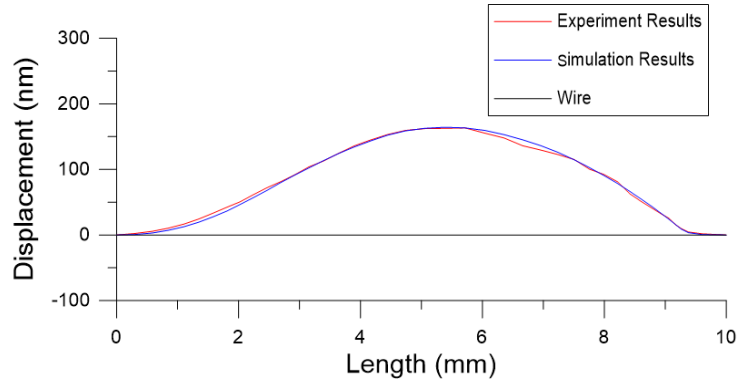
Figure 4.16: First out-of-plane bending mode of CuCorAl wire from top view
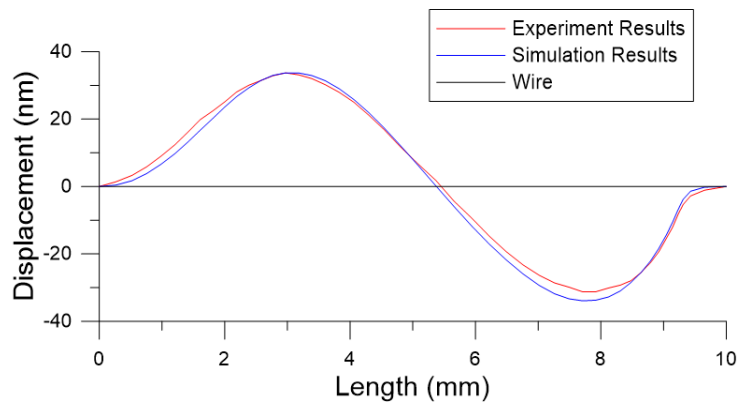
Figure 4.17: Second out-of-plane bending mode of CuCorAl wire from top view

fourth in-plane bending modes of the wire were experimentally measured using laser vibrometer. It is well known that existing only a node (no motions) along the wire at certain frequency corresponds second bending mode. Two and three nodes represent third, and fourth bending modes respectively.
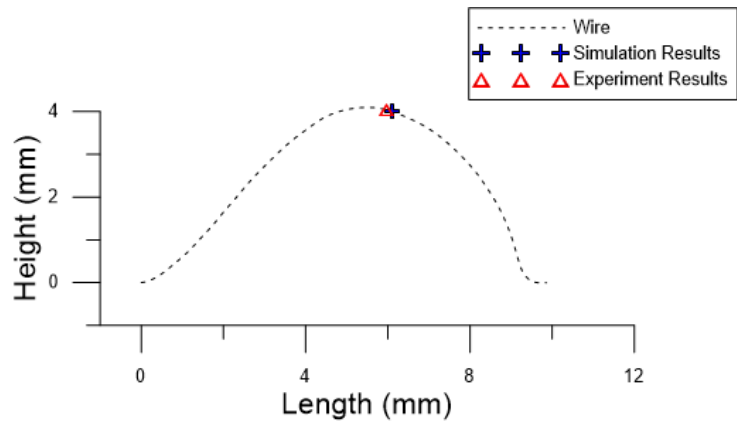
Figure 4.18: Node along wire for second in-plane bending mode

The wire whole span was experimentally scanned to measure nodes along the wire using laser vibrometer while wire excited at 11.8 kHz (second in-plane bending mode obtained from modal analysis), and it was found that a node only exists at this frequency. Figure 4.18 shows the experimentally measured only a node along wire with simulation results.
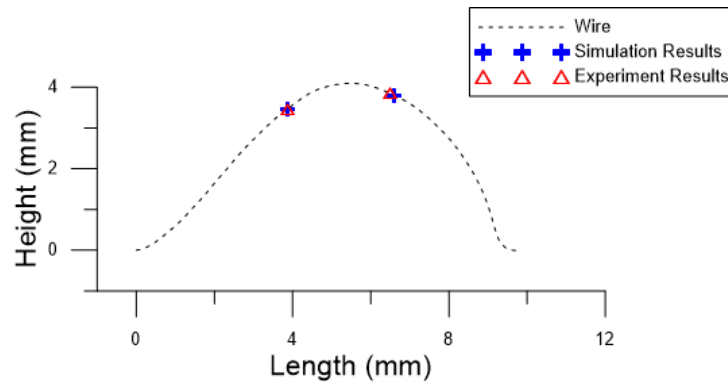
Figure 4.19: Nodes along wire for third in-plane bending mode

Further, This technique was also used for measuring third and fourth in-plane bending modes. Experimentally measured nodes are compared and verified with FEA results. Figures 4.19, and 4.20 show comparison of experimental and simulation results for third and fourth in-plane bending mode shapes of CuCorAl wire from front view. The results are in very good agreement.
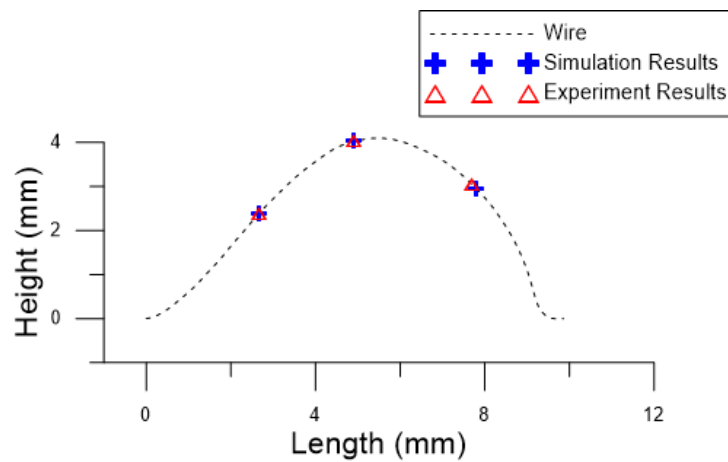
Figure 4.20: Nodes along wire for fourth in-plane bending mode

4.5.2 Frequency Response

Measuring the quality factor of the bonding wires gives information about the damping in the wire. While the Al wire was being excited using thermal actuator, excitation frequency was swept from 5600 to 5980 Hz in small steps, depicted in Figure 4.21.
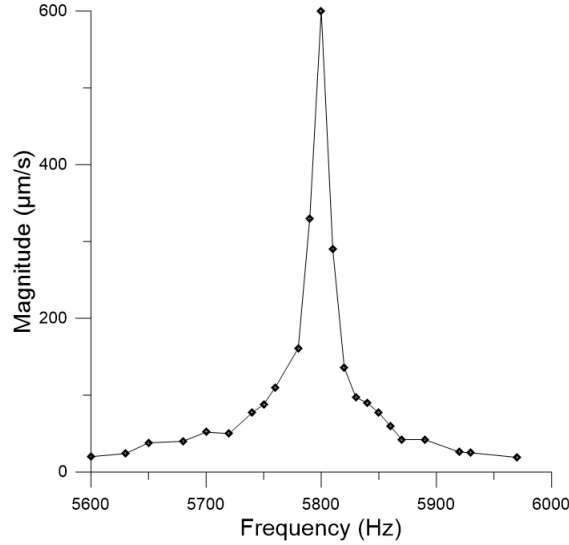
Figure 4.21: First frequency response of Al wire

Relationship between quality factor and damping ratio is given as following;

$$Q = \frac{1}{2\zeta} \tag{4.1}$$

The equation shows that a high quality factor means that the wire is lightly damped, which results in dynamic amplification (large wire responses) when the frequency of excitation is close to resonance. The quality factor of the Al wire for the first mode was calculated using

$$Q_1 = \frac{F_{max}}{F_2 - F_1} = \frac{5800}{5812 - 5788} \tag{4.2}$$

$$= \frac{5800}{24} = 241.67 \tag{4.3}$$

Also the same technique was used to obtain Q_2 of the Al wire at the second
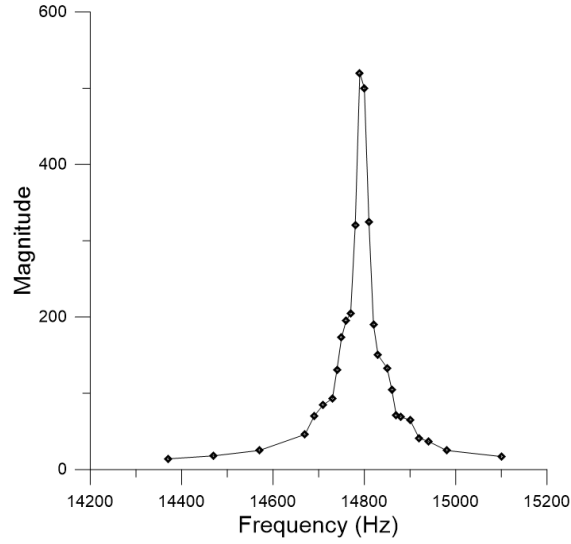
Figure 4.22: Second frequency response of the Al wire

mode as

$$Q_2 = \frac{F_{max}}{F_2 - F_1} = \frac{14790}{14807 - 14783} \tag{4.4}$$

$$Q_2 = \frac{14700}{24} = 616.25 \tag{4.5}$$

According to calculated values of Q_1 and Q_2, the bonding wires have very low damping, which shows that exciting the wires near resonance results in larger amplitude oscillations in the wire which may have an effect on its reliability and lifetime.

Chapter 5

Conclusions and Future Work

5.1 Conclusions

In this thesis, static and dynamic experimental techniques are developed and applied for analysis of thick bonding wires. Analytical and FEA models are also developed to validate and interpret the experimental results. Experimental results are compared with finite element (FEA) and analytical results.

First a static technique is deployed to measure the maximum temperature of the peak point for 11 mm long Al, CuCorAl, and Cu wires. The peak point temperatures are measured for pulse currents with amplitudes of 2, 4, 5, 7, 8, 9, and 10 A and pulse. The measured temperatures agree with those obtained from analytical and FEA models. Results show that the peak point temperature is proportional to the Al content of the wire. The peak temperature of Al wire is higher than that for CuCorAl which, in turn, is higher than that for Cu for all values of DC currents tested.

A transient analysis technique is developed to obtain the time-history of bonding wire displacement under thermal (current) excitation. It is used to measure the peak point displacement for 11 mm long Al, CuCorAl, and Cu wires under pulse currents with amplitudes of 2, 4, 5, 7, 8, 9, and 10 A and pulse width in the range PW=2.5–4.5 s. The experimental time-history of the displacement is used to measure the time constants of 11 mm long Al. The rise time is found to be

0.20 ± 0.016 s and the fall time is found to be 0.07 ± 0.017 s.

Transient analysis is also used to develop a quasi-static technique to measure the steady-state displacement of bonding wire. In this case, the pulse width PW is set to a value one order of magnitude larger than the rise time of wire under test, which allows the wire to settle down to the steady-state static displacement corresponding to the a DC current equal to the pulse amplitude. The quasi-static technique is used to measure the steady-state displacement of 11 mm long Al, CuCorAl, and Cu under 2, 4, 5, 7, 8, 9, and 10 A under DC current. It is found that peak point displacement is proportional to the Al content of the wire. The peak displacement of Al wire is higher than that for CuCorAl which, in turn, is higher than that for Cu for all values of DC currents tested. This indicates that stresses in Cu wire are less than CuCorAl wire which is less than Al wire and that fatigue endurance of Cu wire is better than CuCorAl wire which is better than Al wire.

Experimental dynamic analysis techniques are also developed to conduct modal analysis and harmonic analysis of bonding wire. Firstly, a modal analysis is performed using a solenoid actuator to conduct impact experiments and determine the natural frequencies of the wires. This modal analysis technique is independent of thermal actuation and thermal loading. The technique allows us to measure in-plane and out-of-plane bending modes of the wire. The first five natural frequencies of 11 mm long Al wire are found to be $f_1 = 5.7$ kHz, $f_2 = 14.7$ kHz, $f_3 = 17$ kHz, $f_4 = 33$ kHz, and $f_5 = 34$ kHz. The first five natural frequencies of 10 mm long CuCorAl wire are found to be $f_1 = 4.1$ kHz, $f_2 = 11.8$ kHz, $f_3 = 13.1$ kHz, $f_4 = 25.2$ kHz, and $f_5 = 25.8$ kHz. Through comparison with FEA results, it is found that these modes correspond to the first out-of-plane, second in-plane, second out-of-plane, third in-plane, and third out-of-plane bending modes, respectively, of the wires.

It is noted that the first critical buckling load corresponding to the Al and CuCorAl wires tested, Table 3.3, is tensile due to the aspect ratio of the wire H/L. As a result, the first in-plane bending mode is buckled and cannot be observed in modal analysis experiments. Further, it is found that the experimentally measured

natural frequencies closely agree with those found using FEA and an analytical model for out-of-plane bending.

The drop in the natural frequencies of the wires under thermal loads has also been observed experimentally. The modal analysis technique is used to test wires under thermal loads imposed by DC current passing through the wire. It is experimentally found that even under a maximum current of 10 A DC, the drop in the wire natural frequencies is minimal. For example, the drop in the natural frequencies of CuCorAl wire under 10 A current was measured as 24 Hz, 94 Hz, 213 Hz, and 206 Hz, respectively.

Finally, a technique for harmonic analysis of bonding wire is developed and deployed to verify the natural frequencies of the wire obtained from modal analysis and to evaluate its frequency-response curves. The, frequency-response curves of 11 mm long Al wire in the vicinity of the first out-of-plane and the second in-plane bending modes are used to estimate the quality factor of Al wire for those modes. They are found to be $Q_1 = 241$ and $Q_2 = 616$, demonstrating that the wire is lightly damped. Those high quality factors guarantee large dynamic amplification for current excitations in the vicinity of its first and second natural frequencies.

Harmonic analysis techniques are also employed to experimentally measure in-plane and out-of-plane bending mode shapes of CuCorAl wire. The first and second out-of-plane bending modes are measured and found to agree closely with those obtained from FEA. Further, the experimentally measured nodes of the second, third, and fourth in-plane bending modes are in very good agreement with nodes of the corresponding modes obtained from FEA. This work is the first time that the second out-of-plane bending mode and second, third, and fourth in-plane bending modes of bonding wire are experimentally measured.

The existence of five natural frequencies below 30 kHz for the bonding wire tested is worthy of note. Currents with a frequency content close to any of these frequencies will lead to large displacements, and therefore high heel stresses, in the wire carrying it. This will shorten the wire fatigue life and lead to early failure. Even though IGBT modules in electric vehicles, for example, handle delivery to

motors operating at frequencies below 1 kHz, modern power electronics use chopper circuit that inject frequencies on the order of tens of kHz into the current carried by bonding wire. Thus, it is important to identify the natural frequencies of boding wire and to ensure that the current passing through them is free of harmonics in the vicinity of their natural frequencies to avoid triggering their resonances and, thereby, undermining their reliability.

5.2 Future Work

Our study can provide a good template for analyzing the thin wires. We mostly focused in our study on the dynamic analysis which becomes more critical when thin wires are involved. Since the thin wires were reported to fail when resonating under thermal actuation (for low current) after a couple of minutes [40]. Thus, it is considered that determining natural frequencies and safe operation region for the thin wires can be more critical. Also, the effect of thermal load on natural frequencies for thin wires is expected to be significant. Further, the developed techniques in this study, can be applied for other mechanical applications used in micro electro packaging systems to measure static and dynamic response.

5.3 Published papers

R. Saritas., M. Khater., H. Nafissi., S. Park., T. Dagdelen., E.A. Rahman., M. Yavuz "Modal Response of Bonding Wires under Thermal Loading",*IEEE Nano Conference*, Toronto, Canada, 2014.

T. Dagdelen., S. Park., M. Khater., K. El-Rayes, R. Saritas., E.A. Rahman., M. Yavuz "Fatigue Test for Thick Wire Bonds",*International Conference on Mechanical Vibration and Noise Conference*, Buffalo, New York, USA, 2014.

S. Ozdemir, S. Akhtar, M. E. Khater, O. E. Gunal, R. Saritas, E. Abdel-Rahman, and M. Yavuz, "Measuring the Quality Factor in MEMS Devices," accepted, *Austin Journal of Nanomedicine & Nanotechnology.*

References

[1] A.C. Fischer., J.G. Korvink., N. Roxhed., G. Stemme., U. Wallrabe., and F. Niklaus,"Unconventional applications of wire bonding create opportunities for microsystem integration", *Journal of Micromechanics and Microengineering*, Volume 23, pp. 083001/1-18, 2013.

[2] I. Lum., C.J. Hang.,1 M. Mayer and Y. Zhou, "In Situ Studies of the Effect of Ultrasound During Deformation on Residual Hardness of a Metal", *Journal of Electronic Materials*, Volume 38, pp. 647-654, 2009.

[3] J.E Krzanowski, "A Transmission Electron Microscopy Study of Ultrasonic Wire Bonding", *IEEE Transactions On Components, Hybrids, and Manufacturing Technology*, Volume 13, pp. 176-181, 1990.

[4] Technical Note, by Small Precision Tools,

[5] G. Harman *Wire Bonding in Microelectronics*, McGraw-Hill, New York, 2010.

[6] T. Dagdelen, "Failure Analysis of Thick Wire Bonds", *MASc. Thesis, University of Waterloo*, 2013.

[7] S. Murali., N. Srikanth., C.J. Vath III, "Effect of wire diameter on the thermosonic bond reliability", *Microelectronics Reliability*, Volume 46, pp. 467-475, 2005.

[8] R. Saritas., M. Khater., H. Nafissi., S. Park., T. Dagdelen., E.A. Rahman., M. Yavuz, "Modal Response of Bonding Wires under Thermal Loading", *IEEE Nano Conference*, Toronto, Canada, 2014.

[9] S. Mazzei., M. Madia., S. Beretta., A. Mancaleoni., S. Aparo, "Analysis of Cu-wire pull and shear test failure modes under ageing cycles and finite element modelling of Si-crack propagation", *Microelectronics Reliability*, in Press.

[10] C.J. Hang., C.Q. Wang., M. Mayer., Y.H. Tian., Y. Zhou., H.H. Wang, "Growth behavior of Cu/Al intermetallic compounds and cracks in copper ball bonds during isothermal aging", *Microelectronics Reliability*, Volume 48, pp. 416-424, 2007.

[11] H.G. Kim., S.M. Kim., J.Y. Lee., M.R. Choi., S.H. Choe., K.H. Kim., J.S. Ryu., S. Kim., S.Z. Han., W.Y. Kim., S.H. Lim, "Microstructural evaluation of interfacial intermetallic compounds in Cu wire bonding with Al and Au pads", *Acta Materialia*, Volume 64, pp. 356-366, 2013.

[12] Stitch Bond Enhancement for X-WireTM Insulated Bonding Wire, Technical Note, by Small Precision Tools and Microbonds Inc, 2007.

[13] K.N. Meyyappan, "Failure Prediction of Wire Bonds Due To Flexure ", *Ph.D. Thesis, University of Maryland*, 2004.

[14] Technical Note, Power Systems Design, 2011

[15] J. Goehre., M.S. Ramelow., K.D.Lang., U.GeiBler, "Interface Degradation of Al Heavy Wire Bonds on Power Semiconductors during Active Power Cycling measured by the Shear Test", *CIPS Conference*, Nuremberg, Germany, 2010.

[16] Y.Yamada., Y. Y. Y. N. I. Takaku., Y. Yagi., I. Nakagawa., T. Atsumi., M. Shirai., I. Ohnuma., and K. Ishida, "Reliability of wire-bonding and solder joint for high temperature operation of power semiconductor device", *Microelectronics Reliability*, Volume 47, pp. 2147-2151, 2007

[17] M.M. Guyennet., X. Perpin., M. Piton, "Revisiting power cycling test for better life-time prediction in traction", *Microelectronics Reliability*, Volume 47, pp. 1690-1695, 2007

[18] W.S. Loh., M. Corfield., H. Lu., S. Hogg., T. Tilford., C M. Johnson, "Wire Bond Reliability for Power Electronic Modules - Effect of Bonding Temperature", *Thermal, Mechanical and Multi-Physics Simulation Experiments in Microelectronics and Micro-Systems EuroSime Conference*, 2007.

[19] J. Bielen., J.-J. Gommans., and F. Theunis, "Prediction of high cycle fatigue in aluminum bond wires: A physics of failure approach combining experiments and multi-physics simulations", *in Proc. 7th Int. Conf. EuroSime*, Como, Italy, 2006.

[20] T. Matsunaga. and Y. Uegai, "Thermal Fatigue Life Evaluation of Aluminum Wire Bonds", *Electronics Systemintegration Technology Conference*, IEEE, 2006.

[21] R. Schmidt. and U.Scheuermann, "Separating Failure Modes in Power Cycling Tests", *CIPS conference*, 2012.

[22] L. Merkle., T. Kaden., M.Sonner., A. Gademann., J. Turki., C. Dresbach., and M. Petzold, "Mechanical fatigue properties of heavy aluminium wire bonds for power applications", *In Electronics System-Integration Technology Conference*, IEEE, 2008.

[23] M. Ciappa., and W. Fichtner, "Lifetime prediction of IGBT modules for traction applications", *In Reliability Physics Symposium*, IEEE, 2000.

[24] J.M. Hu., M. Pecht, and A. Dasgupta, "A Probabilistic Approach for Predicting Thermal Fatigue Life of Wire Bonding in Microelectronics", *Journal of Electronic Packaging*, Volume 113, pp. 275-285, 1991

[25] P. A. A. Laura. and P. L. Verniere de Irassar, "A Note on In-Plane Vibrations of Arch-Type Structures of Non-Uniform Cross-Section: The Case of Linearly Varying Thickness", *Journal of Sound and Vibration*, Volume 124, pp.1-12, 1988

[26] F. Yang., R. Sedaghati., and E. Esmailzadeh, "Free in-plane vibration of general curved beams using finite element method", *Journal of Sound and Vibration*, Volume 318, pp.850-867, 2008

[27] T. Tarnopolskaya and F. R. De Hoog, "Low-Frequency Mode Transition in the FreeIn-Plane Vibration of Curved Beams", *Journal of Sound and Vibration*, Volume 228, pp.69-90, 1999

[28] T. M. Wang., R. H. Nettleton, and B. Keita, "Natural frequencies for out-of-plane vibrations of continuous curved beams", *Journal of Sound and Vibration*, Volume 68, pp.427-436, 1980

[29] T.Irie., G. Yamada., and K. Tanaka, "Natural Frequencies of Out-of-Plane Vibration of Arcs", *Journal of Applied Mechanics*, Volume 49, pp. 910-913, 1982

[30] W. Lacarbonara, "A Theoretical and Experimental Investigation of Nonlinear Vibrations of Buckled Beams", *M.S. Thesis, Virginia Polytechnic Institute and State University*, 1997.

[31] M. Khater., T. Dagdelen., A. Abdel-Aziz., S. Park., K. El-Rayes., E. Abdel-Rahman., M. Yavuz, "Analysis of Thick Wire Bonds under Thermal Loads", *The 4th Canadian Conference on Nonlinear Solid Mechanics* , (CanCNSM), Montreal, Canada, 2013.

[32] S.A. Emam, "A Theoretical and Experimental Study of Nonlinear Dynamics of Buckled Beams", *Ph.D. Thesis, Virginia Polytechnic Institute and State University*, 2002.

[33] M. Younis., H. Ouakad., F. Alsaleem., R. Miles., W. Cui, "Nonlinear Dynamics of MEMS Arches Under Harmonic Electrostatic Actuation", *Journal of Microelectromechanical systems*, Volume 19, pp. 647-656, 2010

[34] A. Nayfeh and D. Mook, *Nonlinear Oscillations*, Wiley Interscience, 1979.

[35] M. Younis, E. Abdel-Rahman, and A. Nayfeh, "A Reduced-Order Model for Electrostatically Actuated Microbeam-Based MEMS", *Journal of Microelectromechanical systems*, Volume 12, pp. 672-680, 2003

[36] S. Timoshenko and N. Goodier, *Theory of Elasticity*, 2nd edition, McGraw-Hill, New York, 1951.

[37] J.P. Holman, *Heat Transfer*, McGraw-Hill, New York, 2010.

[38] Tianjin Century Electronics Co., http://www.china-rectifier.com

[39] Heraus Company, http://heraeus-contactmaterials.com/en/products/audr/productpage_smt_adhesives_2.aspx

[40] T.J. Barber., D.G. Charlton., M. Warren., W. Murray., G. Villani., A.R. Weidberg, "Resonant bond wire vibrations in the ATLAS semiconductor tracker", *Nuclear instruments and methods in physics research*, Volume 538, pp. 442-457, 2005